Title

Function and firing of the *Streptomyces coelicolor* contractile injection system requires the membrane protein CisA

Authors

Bastien Casu[1], Joseph W. Sallmen[2], Peter E. Haas[1], Govind Chandra[2], Pavel Afanasyev[3], Jingwei Xu[1], Martin Pilhofer[1,*] and Susan Schlimpert[2,4,*]

Short title

A membrane protein enables *Streptomyces* contractile injection system firing

Affiliations

[1]Department of Biology, Institute of Molecular Biology & Biophysics, Eidgenössische Technische Hochschule Zürich, Otto-Stern-Weg 5, 8093 Zürich, Switzerland

[2]John Innes Center, Department of Molecular Microbiology, Norwich Research Park, Norwich, NR4 7UH, United Kingdom

[3]Cryo-EM Knowledge Hub, Eidgenössische Technische Hochschule Zürich, Otto-Stern-Weg 3, 8093 Zürich, Switzerland

[4]Centre for Microbial Interactions, Norwich Research Park, Norwich, NR4 7UH, United Kingdom

Contact Info

* Correspondence: susan.schlimpert@jic.ac.uk (S.S.) and pilhofer@biol.ethz.ch (M.P.)

Abstract

Bacterial contractile injection systems (CIS) are phage tail-like macromolecular complexes that mediate cell-cell interactions by injecting effector proteins into target cells. CIS from *Streptomyces coelicolor* (CIS^{Sc}) are localized in the cytoplasm. Under stress, they induce cell death and impact the *Streptomyces* life cycle. It remains unknown, however, whether CIS^{Sc} require accessory proteins to directly interact with the cytoplasmic membrane to function.

Here, we characterize the putative membrane adaptor CisA, a conserved factor in *CIS* gene clusters across *Streptomyces* species. We show by cryo-electron tomography imaging and *in vivo* assays that CIS^{Sc} contraction and function depend on CisA. Using single-particle cryo-electron microscopy, we provide an atomic model of the extended CIS^{Sc} apparatus; however, CisA is not part of the complex. Instead, our findings show that CisA is a membrane protein with a cytoplasmic N-terminus predicted to interact with CIS^{Sc} components, thereby providing a possible mechanism for mediating CIS^{Sc} recruitment to the membrane and subsequent firing.

Our work shows that CIS function in multicellular bacteria is distinct from Type 6 Secretion Systems and extracellular CIS, and possibly evolved due to the role CIS^{Sc} play in regulated cell death.

Keywords: bacterial development/cellular microbiology/contractile phage tail-like structures/regulated cell death/multicellularity

41 # Introduction

42 Bacteria employ different types of contractile injection systems (CIS) to mediate cell-cell
43 interactions or cell death (1). CIS are evolutionarily and structurally related to contractile tails
44 of bacteriophages and are comprised of core modules, including a baseplate, a contractile
45 sheath, and an inner tube (2,3). CIS firing is triggered by a conformational change within the
46 baseplate (4,5) and results in the contraction of the sheath, which in turn propels the inner tube
47 along with the spike tip. Tube expulsion facilitates the release of associated effector proteins
48 into target cells or the extracellular space (6,7).

49 Bioinformatic analyses have shown that CISs are conserved across diverse microbial phyla,
50 including Gram-negative and Gram-positive bacteria, as well as archaea (8,9). Based on their
51 distinct modes of action, CIS can be categorized into two main groups: intracellular type VI
52 secretion systems (T6SS) and extracellular CIS (eCIS). T6SS are abundant among Gram-
53 negative bacteria and in some archaea, and they are anchored to the cytoplasmic membrane
54 during assembly and firing (10–12). A crucial component of the T6SS is the baseplate, which
55 acts as a nucleus for T6SS assembly and mediates the binding of the T6SS particles to the
56 cytoplasmic membrane until contraction. Upon contraction, the spike and inner tube are
57 propelled out of the cell into an adjacent cell or the medium. eCIS, on the other hand, are
58 assembled as free-floating particles in the cytoplasm and are subsequently released into the
59 extracellular space upon lysis of the producer cell (13–16). Following the release, eCIS attach
60 to the surface of target cells via their tail fibers, followed by contraction and puncturing of the
61 target cell envelope.

62 Besides T6SS and eCIS, there is accumulating evidence of additional CIS assemblies with
63 distinct modes of action in bacteria. For example, in multicellular cyanobacteria, CIS are
64 anchored to the intracellular thylakoid membrane stacks via an extension of the baseplate
65 components and have been proposed to function in cell lysis and the formation of "ghost cells"
66 in response to stress conditions (17). Furthermore, several recent studies reported the
67 production of free-floating cytoplasmic CIS particles in the multicellular monoderm
68 *Streptomyces* bacteria, which have been shown to modulate cellular development through
69 presumably slightly different mechanisms (18–22).

70 Notably, many *Streptomyces* genomes contain a class IId eCIS locus, a subtype that is
71 structurally less well understood compared to other eCIS subtypes, such as 'antifeeding
72 prophages' (AFPs) from *Serratia*, 'metamorphosis-associated contractile structures' (MACs)
73 from *Pseudoalteromonas luteoviolacea*, AlgoCIS from *A. machipongonensis* or
74 '*Photorhabdus* virulence cassettes' (PVCs) from *P. asymbiotica* (1).

75 *Streptomyces* are best known for producing a plethora of medically and industrially important
76 secondary metabolites, including molecules with antimicrobial, antifungal, anticancer or
77 immunosuppressive properties. The production of these molecules is tightly coordinated with
78 the *Streptomyces* developmental life cycle that encompasses functionally distinct filamentous
79 cell types: vegetative hyphae that grow by tip extension and branching to scavenge for nutrients
80 and reproductive (aerial) hyphae that eventually differentiate into chains of spores, which can
81 then be dispersed to restart the life cycle (23,24). Using *Streptomyces coelicolor* as a model
82 organism, we and others previously demonstrated that *S. coelicolor* CIS (CIS^{Sc}) mediate a form
83 of regulated cell death, which influences the onset of sporulation and secondary metabolite
84 production in response to exogenous stress and unknown cellular signals (Figure 1a) (18,19).

85 It remains unclear, however, whether CIS^{Sc} contraction and firing occurs while the CIS^{Sc}
86 particles are free-floating in the cytoplasm or whether this depends on an interaction with the
87 membrane. Moreover, CIS encoded in *Streptomyces* genomes lack clear homologs for tail fiber
88 components or a T6SS trans-envelope complex, raising the question of how CIS^{Sc} particles
89 could potentially interact with the cytoplasmic membrane. We and others recently noted an
90 uncharacterized protein (18,19), SCO4242, which is conserved in the majority of *Streptomyces*
91 species and other Actinomycete species that carry a type IId eCIS locus (8,9) (Supplementary
92 Fig. 1 and Supplementary Data 1 and 2). Interestingly, SCO4242 is encoded just downstream
93 of the baseplate components in the CIS^{Sc} gene cluster, a location that usually encodes tail fibers
94 from conventional eCIS (13,16,25). We will, therefore, refer to the gene product of SCO4242
95 as CisA for "CIS^{Sc}-associated protein A." Here, we set out to assess the importance of CisA
96 for CIS^{Sc} function and its possible role as a membrane anchor.

97 # Results

98 ## CisA is required for CIS^{Sc} contraction *in situ*

99 To explore the role of CisA (SCO4242) in CIS^{Sc} contraction and function, we first generated a
100 *S. coelicolor* Δ*cisA* null mutant. Negative stain electron microscopy (EM) imaging of CIS^{Sc}
101 particles that were purified from Δ*cisA* mutant cells showed assemblies in the contracted
102 conformation, similar to the CIS^{Sc} particles purified from the wild type (WT) (Fig. 1b/c). Next,
103 to examine the impact of CisA on the behavior of CIS^{Sc} *in situ*, we imaged vegetative hyphae
104 of the WT, the Δ*cisA* mutant and the complemented mutant (Δ*cisA/cisA*$^{+}$) by cryo-electron
105 tomography (cryoET) (270 tomograms in total, n=3 experiments per strain). We previously
106 demonstrated that CIS^{Sc} contraction correlates with the cellular integrity of *S. coelicolor* wild-
107 type (WT) hyphae and showed that in intact hyphae, CIS^{Sc} particles are consistently observed
108 in their extended conformation in the cytoplasm, whereas in partially lysed hyphae, the ratio
109 of extended to contracted particles is approximately 2:1, and dead hyphae only contained fully
110 contracted CIS^{Sc} assemblies (18). Interestingly, and in contrast to the WT and the
111 complemented *cisA* mutant strain (Fig. 1d and f), *cisA*-deficient hyphae only contained CIS^{Sc}
112 particles in the extended conformation irrespective of the cellular integrity of the hyphae (Fig.
113 1e, Supplementary Fig. 2a-d). Moreover, our analysis consistently showed only two CIS^{Sc}
114 conformations in intact and dead hyphae, respectively: the fully extended state (233 nm in
115 length, 18 nm in diameter, n=100 CIS^{Sc} particles) and the fully contracted state (124 nm in
116 length, 23 nm in diameter, n=100 CIS^{Sc} particles). While hyphal cell death can be caused by a
117 range of external or internal factors, our results demonstrate that CIS^{Sc} contraction is not a
118 consequence of cell death and requires CisA *in situ*.

119 ## CryoEM structure of the extended CIS^{Sc} assembly

120 The *S. coelicolor cis* gene cluster consists of 19 predicted open reading frames (accessions
121 *SCO4242-4260*) (Fig. 2a), including genes with sequence similarities to potential CIS
122 structural components (*cis1-cis16*), as well as additional genes with unknown functions
123 (including *cisA*) (18,19). To determine whether CisA is an integral component of CIS^{Sc}, we set
124 out to elucidate the high-resolution structure of purified CIS^{Sc} particles from a non-contractile
125 CIS^{Sc} mutant (18). The purified assemblies were subjected to single-particle cryo-electron
126 microscopy (cryoEM) for structure determination (Supplementary Fig. 3), yielding the first

127 high-resolution model of the CIS^{Sc} in its extended conformation, which also presents the first
128 example of a CIS IId subtype (8).

129 Our model shows that extended CIS^{Sc} particles share the conserved eCIS architecture,
130 including the three core modules: cap, sheath-tube and baseplate (Fig. 2b). We processed the
131 dataset using an established workflow that was previously employed to produce the atomic
132 model for other CIS (Supplementary Fig. 3) (13,17). The resulting maps of the baseplate and
133 the cap reached resolutions of 3.5 and 3.4 Å, respectively. The quality of the final maps from
134 the two modules enabled *de novo* structural modeling (Supplementary Fig. 4, Supplementary
135 Table 1).

136 The final model of CIS^{Sc} comprises 783 polypeptide chains that assemble into a bullet-shaped
137 particle measuring 268 nm in length (Fig. 2b/c). All analyzed particles were identical in length,
138 consistent with our *in situ* data of extended CIS^{Sc} particles in vegetative hyphae of WT
139 *S. coelicolor* (Fig. 1d-f). The length of eCIS particles is often controlled by tape measure
140 proteins (26). We note, however, that the corresponding gene is absent from the CIS^{Sc} gene
141 cluster. The distal end of the CIS^{Sc} is capped by a tail terminator complex (Fig. 2c/e). This cap
142 comprises one protein, Cis16, forming a C6-symmetrical complex that terminates the inner
143 tube and sheath, respectively. This minimal architecture resembles the cap complexes of PVC
144 or Pyocin R2 CISs, but it is different from the more complex AlgoCIS from
145 *A. machipongonensis* and AFP from *S. entomophila* (Supplementary Fig. 5) (13,16,25,27). The
146 structures of the CIS^{Sc} sheath-tube module have been previously discussed, notably showing
147 that the sheath (domains 1/2) contracts by widening and shortening, similar to other CIS (18).
148 We found that the module consists of 61 sheath layers (Cis2-L_1–L_{61}) and 60 tube layers (Cis1-
149 L_1-L_{60}) (Fig. 2b/d). The baseplate module comprises a heteromeric assembly of the proteins
150 Cis1b/7/8/9/11/12 (Fig. 2b/c). The symmetry transition from the inner tube (Cis1a, C6) to the
151 VgrG-like spike (Cis8, C3) is adapted by two layers of the tube initiators Cis1b and Cis7. The
152 first layer of the sheath (Cis2) is bound to the conserved gp25-like protein Cis9, which connects
153 to the baseplate 'wedges' composed of Cis11 and Cis12 (Fig. 2b/c). Importantly, the CIS^{Sc}
154 'wedges' consist of two copies of Cis11 and one copy of Cis12 (Fig. 2f), resembling the
155 baseplate of Pyocin R2(27). This is in contrast to other previously reported eCIS, whose
156 baseplate wedge comprises only one Cis11/12 component (AlgoCIS, AFP, PVC) and a Cis11
157 extension forming a cage around the spike (AlgoCIS) (Supplementary Fig. 6) (13,16,25).
158 Furthermore, we did not detect any structural components that resemble tail fibre proteins. This

159 is in line with the bioinformatic analysis of the *cis* gene cluster (Fig. 2a), suggesting the absence
160 of conventional tail fibre genes.

161 Out of the 19 predicted open reading frames in the CIS^{Sc} gene cluster (Fig. 2a), nine encoded
162 proteins were present in the final reconstruction, for which all atomic models were built (Fig.
163 2b/c). However, we did not detect a density for CisA in our model, suggesting that CisA is not
164 part of purified CIS^{Sc} particles but may interact with them via a different mechanism. This
165 finding is also in agreement with mass spectrometry results, which indicate the absence of CisA
166 peptides from purified CIS^{Sc} particles (Supplementary Table 1) (18). We speculate that the
167 purification protocol used to isolate CIS^{Sc} particles for single-particle analysis may not preserve
168 the CIS^{Sc}-CisA interaction or that the interaction is too transient and only occurs under specific
169 growth conditions. To better understand how CisA mediates CIS^{Sc} function, we further
170 characterized CisA *in vivo*.

171 CisA is a bitopic protein

172 Bioinformatic analyses (18,19) and structural modeling of CisA suggest that CisA consists of
173 a largely unstructured N-terminal region, a transmembrane segment, and a conserved C-
174 terminal domain (CTD) that shares structural similarity to periplasmic substrate-binding
175 domains (Fig. 3a). Additional Alphafold3 (28) modeling using just the ordered C-terminus of
176 CisA, including the transmembrane domain and the CTD (amino acids 285-468), predicts that
177 CisA can oligomerize into a pentamer via the CTD (Fig. 3b and c). These findings suggest that
178 CisA may exist in distinct configurations within the cell. To characterize the intracellular
179 localization of CisA, we first generated a strain in which *cisA* was fused to the N-terminus of
180 *mCherry* and expressed *in trans* from a constitutive promoter in the *S. coelicolor* Δ*cisA* mutant.
181 Using fluorescence light microscopy, we consistently observed a CisA-mCherry fluorescence
182 signal along the hyphal periphery, indicative of a membrane-associated protein (Fig. 3d). In
183 contrast, no fluorescence was observed in WT hyphae carrying an empty plasmid (Fig. 3e).
184 Next, we tested if CisA is indeed localized to the membrane *in vivo* by performing cellular
185 fractionation experiments. We separated soluble proteins from membrane proteins using whole
186 cell lysates from the *S. coelicolor* WT or the Δ*cisA* mutant that was complemented with a *cisA-*
187 *3xFLAG* fusion expressed *in trans* from a constitutive promoter. Our analysis confirmed that
188 CisA-3xFLAG co-sedimented with the cell membranes, while the cytoplasmic transcription
189 factor WhiA could only be detected in the soluble protein fraction (Fig. 3f).

190 Next, we investigated the topology of CisA in the membrane using a dual *phoA-lacZα* reporter
191 system in *E. coli*. The reporter activity can be directly visualized on indicator plates based on
192 the complementary activities of the cytoplasmic reporter β-galactosidase LacZ (magenta
193 coloration) and the periplasmic reporter alkaline phosphatase PhoA (blue coloration) (29). We
194 engineered *E. coli* strains that expressed a C-terminal fusion of CisA variants to the PhoA-
195 LacZα reporter, including full-length CisA and CisA variants that carried either a deletion in
196 the predicted transmembrane domain and/or the putative periplasmic domain (Fig. 3g). In
197 addition, we included three controls, including 1) cells carrying the empty reporter plasmid,
198 resulting only in cytoplasmic β-galactosidase activity, 2) cells expressing a PhoA/LacZ fusion
199 to the *Streptomyces* cytoplasmic cell division protein SepH, and 3) cells expressing a
200 PhoA/LacZ fusion to the periplasmic domain of the *Streptomyces* membrane protein RsbN
201 (30,31). The results of this assay confirmed that CisA is a bitopic protein with an N-terminus
202 (amino acids 1-285) located in the cytoplasm and a C-terminus (amino acids 310-468) present
203 in the periplasm of *E. coli* (Fig. 3h).

204 Collectively, our results demonstrate that CisA is a membrane protein comprised of a flexible
205 cytoplasmic N-terminal domain and a periplasmic C-terminal domain that is predicted to
206 facilitate CisA oligomerization.

207 CisA is essential for the cellular function of CIS^{Sc}

208 We previously established a fluorescence-based assay to show that the production of functional
209 CIS^{Sc} particles results in a significantly reduced viability of *Streptomyces* hyphae exposed to
210 exogenous stress, including treatment with the membrane-pore forming antibiotic nisin, UV
211 radiation or the protonophore carbonyl cyanide 3-chlorophenylhydrazone (CCCP) (18). This
212 viability assay is based on the measurement of the ratio of two fluorescent markers, namely
213 cytoplasmic sfGFP produced by viable intact hyphae and the membrane dye FM5-95 to detect
214 intact as well as partially lysed hyphae. Using this assay, we tested whether CisA was essential
215 for CIS^{Sc}-mediated cell death and determined the relative viability of the WT, the Δ*cisA* and
216 the complemented *cisA* (Δ*cisA/cisA*$^{+}$) strains expressing cytosolic sfGFP. We compared cells
217 exposed to a sublethal concentration of nisin (1 µg/ml for 90 min) to cells not exposed to
218 antibiotic stress. All three strains were found to express CIS^{Sc} assemblies under these growth
219 conditions (Supplementary Fig. 7).

220 Without nisin stress, all three strains exhibited a similar sfGFP/FM5-95 ratio, indicating no
221 significant difference in viability (Fig. 4a/c). As previously observed (18), the viability of the
222 WT was dramatically reduced in response to nisin stress. In contrast, the viability of Δ*cisA*
223 hyphae was unaffected by nisin stress and comparable to the viability of untreated cells. This
224 phenotype could be completely reversed by complementing the Δ*cisA* deletion *in trans* (Fig.
225 4b/d). Notably, the Δ*cisA* strain phenocopies CIS^{Sc} knockout and non-contractile mutants we
226 analyzed previously (18). Thus, we conclude that CisA is required for CIS^{Sc}-mediated cell
227 death upon stress.

228 To further test the dependence of CIS^{Sc} function on CisA, we conducted additional *in vivo*
229 assays. Previous studies showed that the absence of functional CIS^{Sc} impacted the timely
230 differentiation of *Streptomyces* hyphae into chains of spores, resulting in accelerated cellular
231 development and reduced secondary metabolite production (18,19). Here, we repeated these
232 analyses using the WT, the Δ*cisA* mutant and the complemented mutant (Δ*cisA/cisA*$^{+}$). All
233 strains consistently completed their life cycle and synthesized spores after 96 h of growth on
234 solid medium (Fig. 4e). Importantly, unlike the WT and the Δ*cisA/cisA*$^{+}$ strain, Δ*cisA* mutant
235 colonies sporulated markedly earlier (72 h). These findings were further corroborated by
236 quantifying the number of spores produced by each strain under the same experimental
237 conditions (Fig. 4f). Finally, we examined the effect of a *cisA* deletion on secondary metabolite
238 production by quantifying the level of actinorhodin production in *S. coelicolor* (32). Compared
239 to the WT and the complemented mutant strain (Δ*cisA/cisA*$^{+}$), the Δ*cisA* mutant showed
240 significantly reduced levels of actinorhodin production (Supplementary Fig. 8). Our data
241 therefore support the conclusion that the cellular function of CIS^{Sc} in *S. coelicolor* depends on
242 CisA, and its absence impacts the timely cellular and chemical differentiation of *S. coelicolor*
243 hyphae.

244 # Discussion

245 Here, we identify CisA as an essential membrane-associated factor that mediates the cellular
246 function of CIS^{Sc} particles in *Streptomyces coelicolor*. In the absence of CisA, CIS^{Sc} are not
247 able to contract in the cellular context (Fig. 1). Similar to a CIS^{Sc} deletion or non-contractile
248 mutant (18), the deletion of *cisA* decreases the induction of cell death upon stress, which in
249 turn affects cellular development and secondary metabolite production (Fig. 5). The
250 mechanistic aspects of this distinct mode of action of CIS^{Sc} are discussed below.

251 A conserved feature of all previously studied CIS is the requirement of the contractile apparatus
252 to bind to a membrane before firing. This can be achieved in various ways, resulting in the
253 classification of CIS into distinct modes of action. First, T6SS are anchored to the cytoplasmic
254 membrane of the host cell by a trans-envelope complex spanning from the cytoplasm to the
255 inner membrane, periplasm, and outer membrane (33–35). Second, contractile phages and eCIS
256 bind to the surface of their target cell via tail fibers, which are typically connected to the
257 baseplate and transmit the signal for firing to the baseplate (13,16,36). Third, tCIS are anchored
258 to thylakoid membrane stacks in cyanobacteria by an extension of their baseplate (17). Finally,
259 and in contrast to the previously described CIS, we demonstrate that intracellular CIS^{Sc}
260 particles from *Streptomyces* do not contain structural components that can directly bind to the
261 host membrane. Our data suggest that CisA is required to mediate an interaction of CIS^{Sc} with
262 the cytoplasmic membrane prior to firing (Fig. 5). This interaction may occur directly via the
263 binding of the CIS^{Sc} particle to the membrane protein CisA, or through the interaction with a
264 yet unknown factor. To explore this idea, we performed an *in silico* prediction of protein-
265 protein interactions between monomeric CisA and CIS^{Sc} components using Alphafold2-
266 Multimer (37) (Supplementary Fig. 9a). Interestingly, this analysis identified the baseplate
267 component Cis11 as a significant hit and possible interaction partner of CisA (Supplementary
268 Fig. 9b-d). Importantly, such a protein-protein interaction would be consistent with our
269 cryoEM structure (Fig. 2b-f), which shows a peripheral surface-exposed position of Cis11 in
270 the baseplate complex of extended CIS^{Sc}.

271 Additional structural modeling with truncated versions of CisA in complex with Cis11 further
272 support the idea that the largely unstructured cytosolic portion of CisA is required to interact
273 with the Cis11 (Supplementary Fig. 10). We have been unable to confirm a direct interaction
274 between CisA and Cis11 because the expression of *cisA* is toxic in *E. coli,* which prevented the

275 experimental analysis of the CisA-Cis11 interaction using co-purification approaches and
276 bacterial two-hybrid studies. While we currently cannot exclude the possibility that the
277 proposed CisA-Cis11 interaction involves an additional unknown factor, we did detect CisA
278 peptides in crude purifications of CIS^{Sc} from nisin-stressed cells (Supplementary Table 2). This
279 would be consistent with a transient and/or short-lived interaction of CIS^{Sc} particles with the
280 membrane and CisA. In agreement with this idea, we rarely observed extended CIS^{Sc}
281 assemblies associated with the cytoplasmic membrane via their baseplate in WT cells (Fig. 1d).

282 We further speculate that CisA may not only serve as a mediator for the interaction of CIS^{Sc}
283 with the cytoplasmic membrane but also as a sensor and checkpoint for inducing cell death
284 under specific stress conditions or in response to cellular signals. Notably, protein structure
285 searches with Foldseek (38) using just the conserved extra-cytoplasmic C-terminal CisA
286 domain (amino acids 310-468) suggest that this domain shares similarity with protein solute-
287 binding protein domains. Thus, the C-terminal CisA domain could potentially be involved in
288 directly or indirectly sensing stress signals. Recognition or binding of such a signal by
289 monomeric CisA could trigger a conformational change that results in CisA oligomerization,
290 which in turn could lead to an "activated" CisA configuration that is primed to mediate the
291 recruitment of CIS^{Sc} assemblies to the cytoplasmic membrane, followed by firing.

292 It is conceivable that the lethal consequences of CIS^{Sc} firing for the producing cell may have
293 driven the evolution of a stepwise mechanism, involving a checkpoint that prevents self-
294 inflicted cell death by accidental firing. Such a stepwise mechanism would ensure that the
295 CIS^{Sc} remain in a free-floating, and safe state within the cytoplasm until a stress signal induces
296 CisA-mediated CIS^{Sc} contraction.

297 METHODS

298 Bacterial strains, plasmids, and oligonucleotides

299 Bacterial strains, plasmids, and oligonucleotides used in this study are listed in Supplementary
300 Tables 3-4. Plasmids were generated using either standard restriction-ligation or assembled
301 using the Gibson Assembly Master Mix (NEB) or *In Vivo* Assembly. All plasmids were
302 verified by DNA sequencing. *Escherichia coli* strains were cultured in LB, SOB, or DNA
303 medium. *E. coli* strains TOP10, DH5α and NEB5α were used to propagate plasmids and

304 cosmids, *E. coli* strain BW25113/pIJ790 for recombineering cosmids and *E. coli*
305 ET12567/pUZ8002 for interspecies conjugation. When required, media was supplemented
306 with antibiotics at the following concentrations: 100 µg/ml carbenicillin, 50 µg/ml apramycin,
307 50 µg/ml kanamycin, 50 µg/ml hygromycin.

308 *Streptomyces coelicolor* strains were cultivated in LB, TSB, TSB-YEME, or R2YE liquid
309 medium at 30 °C in baffled flasks or flasks with springs, at 250 rpm or grown on LB, SFM,
310 R2YE medium solidified with 1.5 % (w/v) Difco agar (39). Antibiotics were added at the
311 following concentrations: 25 µg/ml apramycin, 50 µg/ml kanamycin, 25 µg/ml hygromycin,
312 12.5 µg/ml nalidixic acid.

313 Construction of the *S. coelicolor* Δ*cisA* mutant

314 The λ RED homologous recombination system was used to isolate gene replacement mutations
315 using PCR-directed mutagenesis (ReDirect) of the *S. coelicolor* cosmid StD8A containing the
316 *cis* gene cluster(40),(41). The *cisA* coding sequence (*SCO4242*) was replaced with the
317 *aac3(IV)-oriT* resistance cassette from pIJ773. The mutant cosmid (pSS684) was introduced
318 into *E. coli* ET12567/pUZ8002, followed by conjugation into *S. coelicolor* M145.
319 Exconjugants that had successfully undergone double-homologous recombination were
320 identified by screening for apramycin resistance and kanamycin sensitivity. The deletion of *cisA*
321 was subsequently verified by PCR.

322 Sheath preparation of CIS^{Sc}

323 *S. coelicolor* strains were grown in 30 ml TSB, TSB-YEME or R2YE liquid medium for 48 h.
324 Cells were pelleted by centrifugation (7,000 x g, 10 min, 4 °C), resuspended in 5 ml lysis buffer
325 (150 mM NaCl, 50 mM Tris-HCl, 0.5× CellLytic B (Sigma-Aldrich), 1 % Triton X 100, 200
326 µg/ml lysozyme, 50 µg/ml DNAse I, pH 7.4), and incubated for 1 h at 37 °C. Cell debris was
327 removed by centrifugation (15,000 × g, 15 min, 4 °C) and cleared lysates were subjected to
328 ultra-centrifugation (150,000 × g, 1 h, 4 °C). Pellets were resuspended in 150 µl resuspension
329 buffer (150 mM NaCl, 50 mM Tris-HCl, supplemented with protease inhibitor cocktail
330 [Roche], pH 7.4). CIS^{Sc} sheath preparations were analyzed by negative stain EM imaging (42)
331 and mass spectrometry at the Functional Genomics Center Zürich.

332 To purify non-contractile CIS^{Sc} particles from *S. coelicolor (*SS393*)*, cleared cell lysates were
333 subjected to ultracentrifugation using a sucrose cushion (20 mM Tris pH 8.0, 150 mM NaCl,
334 50 mM EDTA, 1 % Triton X 100, 50 % [w/v] sucrose) (18). The sucrose cushion alongside 1
335 mm of liquid above and residual bacterial contaminants were removed by centrifugation at
336 15,000 x g. Samples were then subjected to a second round of ultracentrifugation without a
337 sucrose cushion (150,000 × g, 1 h, 4 °C) and resulting cell pellets were resuspended in buffer
338 (50 mM Tris, 150 mM NaCl). These crude samples were then further purified by gradient
339 ultracentrifugation (10-50 % continuous gradient made with BIOCOMP gradient master IP
340 model 107 gradient forming instrument) at 100,000 x g for 1 h using a SW55 Ti rotor. The
341 gradient was analyzed in 11 fractions of 500 µl, which were imaged by negative stain EM. The
342 fractions, which contained CIS^{Sc} particles, were pooled and used for further experiments.

343 Negative stain electron microscopy

344 4 µl of purified CIS^{Sc} sheath particles were adsorbed to glow-discharged, carbon-coated copper
345 grids (Electron Microscopy Sciences) for 60 s, washed twice with milli-Q water and stained
346 with 2 % phosphotungstic acid for 45 s. The grids were imaged at room temperature using a
347 Thermo Fisher Scientific Morgagni transmission electron microscope (TEM) operated at
348 80 kV.

349 Mass spectrometry analysis

350 To confirm the presence of predicted CIS^{Sc} components, isolated sheath particles were
351 subjected to liquid chromatography–mass spectrometry analysis (LC–MS/MS). These
352 experiments were conducted at the Functional Genomics Center Zürich. First, the samples were
353 digested with 5 µl of trypsin (100 ng/µl in 10 mM HCl) and microwaved for 30 min at 60 °C.
354 The samples were then dried, dissolved in 20 µl ddH_20 with 0.1 % formic acid, diluted in 1:10
355 and transferred to autosampler vials for liquid chromatography with tandem mass spectrometry
356 analysis. A total of 1 µl was injected on a nanoAcquity UPLC coupled to a Q-Exactive mass
357 spectrometer (ThermoFisher). Database searches were performed by using the Mascot
358 swissprot and tremble_streptomycetes search programs. For search results, stringent settings
359 have been applied in Scaffold (1 % protein false discovery rate, a minimum of two peptides
360 per protein, 0.1 % peptide false discovery rate). The results were visualized by Scaffold
361 software ([Proteome Software Inc.], Version 4.11.1).

362 ## Protein gel electrophoresis and western blotting

363 For general protein analysis, protein samples were boiled at 95 °C for 5 min and separated by
364 a 4–20% Mini-PROTEAN® TGX Stain-Free™ SDS PAGE (BioRad) or 12 % Tris-Glycine
365 SDS PAGE (Invitrogen) and visualized using InstantBlue Coomassie Protein Stain or
366 ReadyBlue Protein Gel Stain (Sigma Aldrich).

367 For western blotting, cells were grown in biological triplicate for 48 h in TSB, 2 ml aliquots of
368 each culture were pelleted and washed once with 1x PBS. Cell pellets were resuspended in 0.4
369 ml of sonication buffer (20 mM Tris pH 8.0, 5 mM EDTA, 1x EDTA-free protease inhibitors
370 [Sigma Aldrich]) and subjected to sonication at 4.5-micron amplitude for 7 cycles of 15 s on /
371 15 s off. Samples were centrifuged at 17,000 x *g* for 15 min at 4 °C. Protein concentration in
372 cleared cell lysate supernatants was determined by Bradford Assay (Biorad). Equivalent total
373 protein concentrations (1 mg/ml) were assayed using the semi-dry western blot transfer. The
374 gel was transferred to a PVDF membrane (Biorad) and probed with the appropriate antibody
375 diluted in TBS-T or using the iBIND buffer system (Thermo Fisher): Rabbit anti-FLAG
376 ([Sigma Aldrich] F7425, 1:2500), Rabbit anti-WhiA ((43), 1:2500), and Goat Anti-Rabbit-
377 HRP (Abcam Ab6721, 1:5000). To visualize HRP-conjugated antibodies, membranes were
378 incubated with SuperSignal West Femto ECL solution (Thermo Fisher).
379

380 ## Cellular fractionation

381 To fractionate membrane and soluble proteins from *S. coelicolor* (WT, SS576), cells were
382 grown for 48 h in 50 ml TSB/YEME and the entire culture volume was pelleted by
383 centrifugation. Cell pellets were resuspended in 1/10 volume of lysis buffer (0.2 M Tris-HCl,
384 pH 8, 10 mg/mL lysozyme, and 1× EDTA-free protease inhibitors; [Roche]), incubated for 30
385 min at 37 °C, and then briefly cooled on ice before lysed by sonication (11 x 15 sec on/off at
386 50 % power at 8 microns on ice). Cell debris was removed by centrifugation at 16,000 × g for
387 20 min and the supernatant was subsequently subjected to two additional rounds of
388 centrifugation. The cleared cell lysate was subjected to ultracentrifugation for 1 h at 150,000 ×
389 g at 4 °C to separate the soluble proteins from membrane proteins. Sedimented membrane
390 proteins were resuspended and washed twice in 1 volume of wash buffer (60 mM Tris-HCl,
391 200 mM NaCl, pH 8, 0.2 mM EDTA, and 0.2 M sucrose) at 150,000 × g at 4 °C for 1 h. The

392 wash step was repeated one final time with the wash buffer containing 8 M urea to remove
393 traces of membrane-associated proteins (44). The final pellet was dissolved in 1/10 of the initial
394 volume with wash buffer (no urea). Equi-volume amounts of fractions were mixed with 2x
395 SDS sample buffer and analyzed by immunoblotting.

396 Membrane protein topology analysis in *E. coli*

397 The coding sequence of CisA was inserted in the dual pho-lac reporter plasmid pKTop, which
398 consists of an *E. coli* alkaline phosphatase fragment $PhoA_{22-472}$ fused in frame after the α-
399 fragment of β-galactosidase $LacZ_{4-60}$ (Supplementary Table 3) (29). For membrane protein
400 topology, *E. coli* TG1 was transformed with the pKTop and derivatives. Membrane protein
401 topology was assayed by plating the resulting reporter strains on dual-indicator plates
402 containing LB agar supplemented with 80 µg/ml 5-bromo-4-chloro-3-indolyl phosphate
403 disodium salt (X-Phos) (Sigma Aldrich, RES1364C-A101X) and 100 µg/mL 6-chloro-3-
404 indolyl-β-d-galactoside (Red-Gal) (Sigma Aldrich, B6149) as indicators, 1 mM IPTG, and 50
405 µg/ml kanamycin. A periplasmic or extracellular location of the reporter fusion results in higher
406 alkaline phosphatase activity (blue color), whereas a cytosolic location of the reporter leads to
407 higher β-galactosidase activity (magenta color). Plates were incubated for two days at 37 °C
408 and then scanned.
409

410 Vitrified sample preparations

411 For single-particle cryoEM (SPA), the *S. coelicolor* non-contractile CIS particles were purified
412 as described above and vitrified using a Vitrobot Mark IV (Thermo Fisher Scientific). 4 µl of
413 samples were applied twice on glow-discharged 200 mesh Quantifoil copper grids (R 2/2)
414 which were manually coated with a layer of 1 nm carbon. Grids were blotted for 5.5 s and
415 plunge-frozen in liquid ethane-propane mix (37 %/63 %). Frozen grids were stored in liquid
416 nitrogen until loading into the microscope.

417 For cryo-electron tomography (cryoET), *Streptomyces* cells were mixed with 10 nm Protein A
418 conjugated colloidal gold particles (1:10 v/v, [Cytodiagnostics]) and 4 µl of the mixture was
419 applied to a glow-discharged holey-carbon copper EM grid (R2/1 or R2/2, [Quantifoil]). The
420 grid was automatically blotted from the backside for 4-6 s in a Mark IV Vitrobot by using a

421 Teflon sheet on the front pad, and plunge-frozen in a liquid ethane-propane mixture (37 %/63
422 %) cooled by a liquid nitrogen bath.

423 SPA data collection and image processing

424 44,925 movies were collected on Titan Krios microscope (Thermo Fisher Scientific), operated
425 at 300 keV equipped with K3 direct electron detector, operating in counting mode, and using
426 a slit width of 20 eV on a GIF-Quantum energy filter (Gatan). The automated data collection
427 was conducted with EPU software (Thermo Fisher Scientific) with a final pixel size of
428 1.065Å/pix over 40 frames with a total dose of 50 $e^-/Å^2$. The targeted defocus was set between
429 -1.6 and -2.8 µm with 0.2 µm increment.

430 Movie-alignments with dose-weighting were performed in MotionCor2 software (45) with a
431 gain reference estimated a posteriori (46) followed by standard in-house pipeline of manual
432 inspection and selection of 38,845 micrographs (47) for further processing in cryoSPARC
433 package v4.0.3 (48). Due to the low concentration of particles and the presence of other
434 contaminants in the sample, automatic particle picking appeared challenging, and we
435 developed a CIS-specific approach for efficient picking of the cap and baseplates. In this
436 approach, CIS^{Sc} particles were manually selected as filaments (start-to-end) on 920
437 micrographs and used for training a crYOLO (49) picking model (Supplementary Fig. 2). The
438 large size of the training set appeared essential for successful picking; we could not get rid of
439 large number of false-positive picks, but there were not so many false-negative picks. Then,
440 CIS^{Sc} particles were picked in crYOLO as filaments, followed by the extraction of the ends of
441 the "filaments" using star_modif.py script (47). Particle coordinates were imported in
442 cryoSPARC, where 211,041 particles were extracted at a large box size of 756 pixels and
443 binned to 64 pixels for initial 2D-classification, which allowed us to separate initial particle
444 sets corresponding to the CIS^{Sc} cap (36,569 particles) and CIS^{Sc} baseplate (43,087 particles)
445 (Supplementary Fig. 2).

446 Two subsets of this dataset were processed separately in cryoSPARC. For the cap subset, a
447 standard cryoSPARC single-particle processing approach was applied, including gradual
448 iterative 2D-classification rounds, followed by selection of good classes and particle re-
449 extraction at finer sampling. The main challenge was the proper centering of the particles
450 selected on the end of elongated filament-like objects with repeating patterns (sheath-tube
451 module of CIS), hampering the alignments. Ab-initio model generation with applied C6

452 symmetry was hampered by poor centering of 2D-classes due to elongated nature of the
453 particles (Supplementary Fig. 2). Homo-refinement with this reference was performed
454 followed by particle re-extraction and one more round of ab-initio model generation with
455 applied C6 symmetry (Supplementary Fig. 2). The new 3D-reconstruction appeared reliable
456 and was used for further iterative 3D-refinements (Homo-refinement and NU-refinements)
457 accompanied by 2D-classification and CTF-refinement rounds to exclude particles with wrong
458 Euler angle assignments. The final 3.4 Å resolution map with imposed C6 symmetry resulted
459 from 19,218 particles.

460 The baseplate subset was processed using the same approach, resulting in a 3D reconstruction
461 with imposed C6 symmetry with a resolution of 3.5Å from 22,980 particles (Supplementary
462 Fig. 2). The tip of the baseplate has a C3 symmetry, therefore to solve that part of the map
463 correctly, we exported that particle stack to Relion4 (50) and took advantage of 2D-
464 classification in Relion to select 18,124 particles, corresponding to the best 2D class averages.
465 3D-refinement with relaxed symmetry resulted in a 3.8 Å 3D-resolution reconstruction with
466 imposed C3 symmetry.

467 Cryo-electron tomography

468 Intact *Streptomyces* cells were imaged by cryoET as described previously (51). Images were
469 recorded using a Titan Krios 300 kV microscope (Thermo Fisher Scientific) equipped with a
470 Quantum LS imaging filter operated at a 20 eV slit width and with K3 Summit direct electron
471 detectors (Gatan). Tilt series were collected using a bidirectional tilt-scheme from -60 to +60°
472 in 2° increments. Total dose was 130-150 $e^-/Å^2$ and defocus was kept at -8 µm. Tilt series were
473 acquired using SerialEM (52), drift-corrected using alignframes, and reconstructed using
474 IMOD program suite (53). To enhance contrast, tomograms were deconvolved with a Wiener-
475 like filter 'tom_deconv' (54).

476 Structural modeling of the CIS^{Sc} complex

477 The map qualities of different modules of CIS^{Sc} (cap and baseplate) allowed for *de novo*
478 structural modeling (Supplementary Fig. 2-3). The atomic models of SCO4243-4248,
479 SCO4252-4253 and SCO4260 were built *de novo* using COOT (55). The resulting models were
480 iteratively refined using RosettaCM (56) and real-space refinement implemented in PHENIX
481 (57). In cases where protein domains could only be partially modeled, side chains were not

482 assigned. Final model validation was done using MolProbity (57) and correlation between
483 models and the corresponding maps were estimated using mtriage (57). To illustrate the
484 complete CIS^{Sc} structure, we generated a composite model by integrating symmetry-related
485 protein subunits into a full model of the CIS^{Sc}, based on the consistent CIS^{Sc} length observed
486 both *in situ* and *in vitro* (Fig. 2b).

487 Fluorescence microscopy

488 Fluorescence-based cell viability assays were performed as described previously (18). Briefly,
489 to produce cytoplasmic sfGFP in *Streptomyces*, the coding sequence for sfGFP was introduced
490 downstream of the constitutive promoter *ermE** on an integrating plasmid (pIJ10257). The
491 plasmid was introduced by conjugation to *S. coelicolor* strains (SS430, SS575, SS576). An
492 equal level of cytoplasmic sfGFP in the different strains was confirmed by Western blotting
493 (Supplementary Fig. 11). *Streptomyces* strains were grown in 30 ml of TSB liquid culture at
494 30 ˚C with shaking at 250 rpm for 48 h. Where appropriate, nisin was added to a final
495 concentration of 1 µg/ml 90 min prior to imaging. One ml aliquots of each culture were
496 vortexed for 1 min to break up mycelial clumps, centrifuged for 5 min at 15,000 x *g*, washed
497 twice with 1xPBS, resuspended in 1 ml of 1xPBS containing 5 µg/ml of the red-fluorescent
498 membrane dye FM5-95 (Invitrogen) and then incubated in the dark at room temperature for 10
499 min followed by two wash steps with 1x PBS. Washed cell pellets were resuspended in a total
500 volume of 50 µl PBS and 10 µl of each sample was spotted onto 1 % agarose pads and
501 subsequently imaged using the Thunder imager 3D cell culture microscope (Leica). First, tile
502 scan images were acquired using the Las X Navigator plug-in software (Leica Application
503 Suite X, Version 3.7.4.23463), and 100 regions of interest were picked manually. Then Z-stack
504 images were acquired using a HC PL APO 100x objective with the following excitation
505 wavelengths: GFP (475 nm) and TRX (555 nm). Images were processed using LasX software
506 to apply thunder processing and maximum projection and FIJI to create segmentation and
507 quantify the live (sfGFP)/total cells (FM5-95) area ratio (58). Statistical analyses were
508 performed on data from biological triplicates (n=100 images for each experiment) using a one-
509 way ANOVA and Tukey's post-test in GraphPad Prism 9 (Version 9.3.1).

510 For imaging the subcellular localization of the CIS adaptor protein in *Streptomyces*, cells (strain
511 JS69 or *S. coelicolor* M145) were grown for 48 h in TSB/YEME liquid medium. Two µl of
512 each strain were spotted on 1 % agarose pads made with water and subsequently imaged.

513 Images were acquired using a Zeiss Axio Observer Z.1 inverted epifluorescence microscope
514 fitted with a sCMOS camera (Hamamatsu Orca FLASH 4), a Zeiss Colibri 7 LED light source,
515 and a Hamamatsu Orca Flash 4.0v3 sCMOS camera. mCherry fluorescence was detected using
516 an excitation/emission bandwidth of 577–603 nm/614–659 nm. Images were collected using
517 Zen Blue (Zeiss) and analyzed using Fiji (58).

518 Cover glass impression of *Streptomyces* spore chains

519 Spore titers of relevant strains were determined by dilution plating (18). 10^7 colony-forming
520 units (CFU) of *S. coelicolor* strains (WT, SS539, SS557) were spread onto R2YE agar plates
521 and grown at 30 °C. Sterile glass coverslips were gently applied to the top surface of each
522 bacterial lawn after 48 h, 72 h and 96 h post inoculation. Coverslips were then mounted onto
523 glass microscope slides and imaged using a 40x objective on a Leica Thunder Imager 3D Cell
524 Culture. Images were processed using FIJI (58).

525 Actinorhodin production assay

526 *S. coelicolor* strains (WT, SS539, SS557) were inoculated into 30 ml R2YE liquid media at a
527 final concentration of 1.5 x 10^6 CFU/ml. Cultures were grown in baffled flasks at 30 °C
528 overnight. Cultures were standardized to an OD_{450} of 0.5 and inoculated in 30 ml of fresh R2YE
529 liquid medium. For the quantification of total actinorhodin production, 480 µl of samples were
530 collected at the indicated time points. 120 µl of 5M KOH was added, samples were vortexed
531 and centrifuged at 5,000 x *g* for 5 min. The weight of each tube was recorded. A Synergy 2
532 plate reader (BioTek) was used then to measure the absorbance of the supernatant at 640 nm.
533 The absorbance was normalized by the weight of the wet pellet.

534 Structure prediction and in silico protein-protein interaction screen

535 CisA structural models (monomer and oligomers) and the CisA-Cis11 complex were predicted
536 using AlphaFold3 (28) and further processed using UCSF Chimera (59) or ChimeraX-1.7.1
537 (60).

538 A pairwise *in silico* screen for possible interactions between CisA and components encoded
539 by the *S. coelicolor cis* gene cluster (*SCO4242-SCO4260*) was conducted using the AlphaFold2
540 Multimer-based LazyAF pipeline (37,61,62). The confidence metric (ipTM) for the top model

541 from each pairwise interaction was tabulated and visualised using Prism (Version 10.2.2) with
542 ipTM scores >0.7, indicating a possible protein-protein interaction (63).
543

544 Bioinformatic analysis of CisA homologs

545 To identify CisA homologs, we performed a reciprocal BLAST search in 120 genomes of
546 *Streptomyces* and other *Actinomycete* species that were previously reported to include a type
547 IId eCIS (8,19) using the closely related *cisA* homologue from *Streptomyces albus* J1074
548 (YP_007743954.1) as a query (72% identical to CisA from *S. coelicolor*) (Supplementary Data
549 1). Of these 120 genomes, 75 had a reciprocal hit for CisA (Supplementary Data 2). Protein
550 sequences of CisA homologs were aligned using Clustal Omega (64) and visualized with
551 JalView (Version 2.11.3.3).
552

553 Data availability

554 Representative reconstructed tomograms (EMD-50935, EMD-50939, EMD-50940, EMD-
555 50944, EMD-50948, EMD-50949) and SPA cryoEM maps (EMD-51564, EMD-51565 and
556 EMD-51566) have been deposited in the Electron Microscopy Data Bank. Atomic models
557 (PDB: 9GTP, PDB: 9GTR, PDB: 9GTS) have been deposited in the Protein Data Bank.

Acknowledgements

We thank ScopeM for instrument access at ETH Zürich. We thank the Functional Genomics Center Zürich for mass spectrometry support. Pilhofer Lab members are acknowledged for discussions. M.P. was supported by the Swiss National Science Foundation (31003A_179255/310030_212592), the European Research Council (679209), and the NOMIS foundation. Work in the lab of S.S. was supported by a Royal Society University Research Fellowship (URF\R1\180075 and URF\R\231009) and BBSRC grant BB/T015349/1 to S.S. and by the BBSRC Institute Strategic Program grant BB/X01097X/1 to the John Innes Centre.

Author contributions statement

B.C., S.S. and M.P. conceived the project. B.C. optimized the sample preparation for SPA; B.C. and P.A. collected and processed the cryoEM data, reconstructed the cryoEM map; B.C., P.E.H. and J.X. built and refined the structural models; B.C. and P.E.H. conducted and processed cryoET; B.C. conducted automated fluorescent light microscopy, determined sporulation efficiency and actinorhodin production; J.W.S. and S.S. generated plasmids and *Streptomyces* strains; J.W.S. performed membrane topology assays, cellular fractionation experiments and imaged strains expressing fluorescently tagged CisA. S.S. and G.C. performed bioinformatic analyses. B.C., J.W.S., S.S. and M.P. wrote the manuscript.

Competing interests statement

The authors declare no competing interests.

578 **Figures and figure legends**

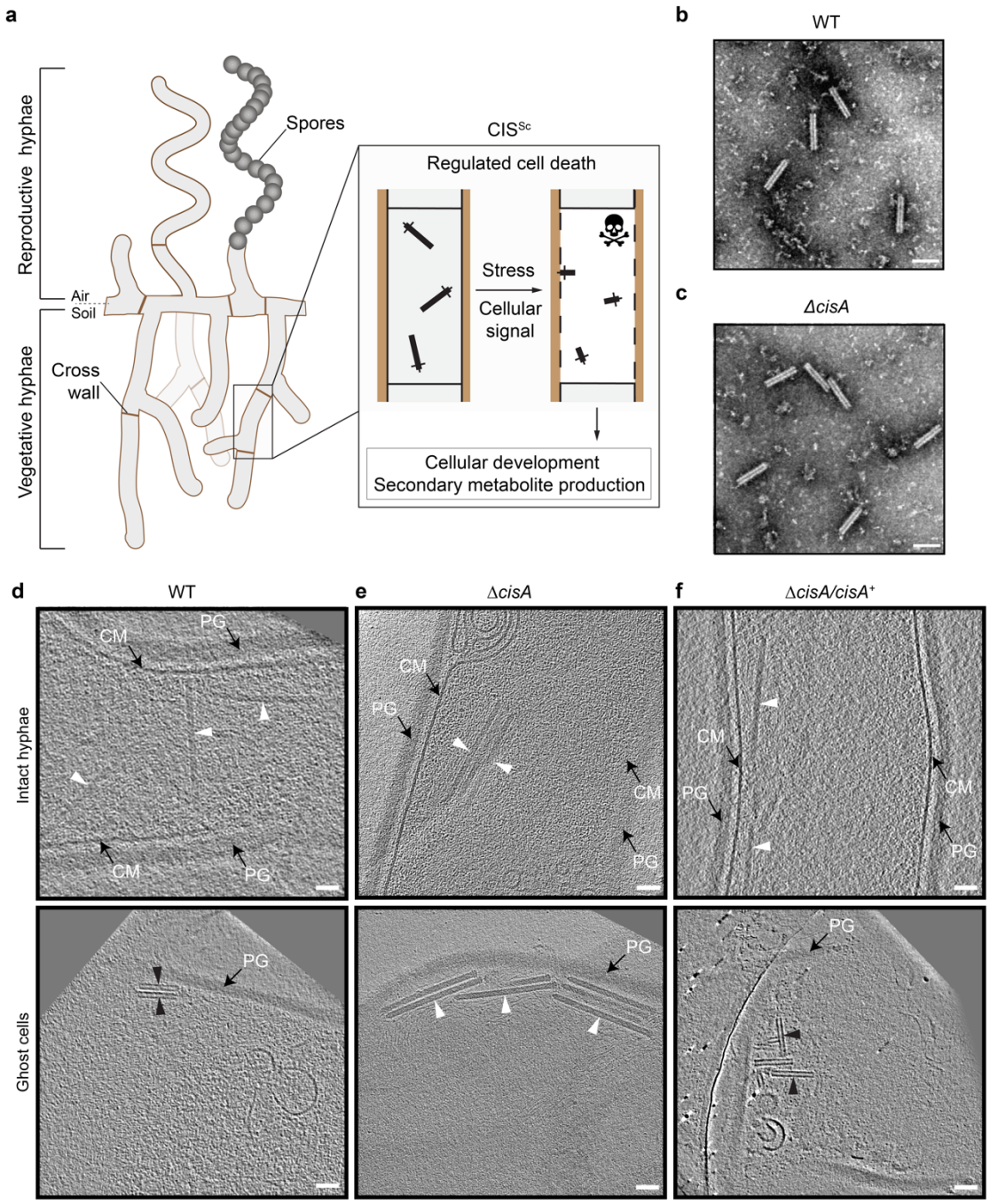

579

580 **Figure 1: Contraction of CIS^{Sc} *in situ* is dependent on CisA.**

581 **a.** Schematic of the mode of action of CIS^{Sc} in *Streptomyces coelicolor* (18,19). CIS^{Sc} are
582 assembled as free-floating particles in the cytoplasm of vegetative hyphae. In response to
583 extracellular stress and/or an unknown cellular signal, CIS^{Sc} particles contract, which results
584 in regulated cell death (mediated by released effectors) and impacts cellular development.

585 **b/c.** Negative-stain electron micrographs of purified CIS^{Sc} particles from *S. coelicolor* wildtype
586 (WT) (b) and the Δ*cisA* mutant (c), show that all CIS^{Sc} particles are functional and contract
587 upon purification. Experiments were performed three independent times. Bars, 100 nm.

588 **d-f.** Shown are representative images of cryo-electron tomogram slices (thickness 11 nm) of
589 vegetative hyphae (top: intact cells; bottom: ghost cells) of *S. coelicolor* WT (d), Δ*cisA* mutant
590 (e), and the complemented Δ*cisA/cisA*$^{+}$ mutant (f). CIS^{Sc} particles remain almost exclusively
591 in an extended state (white arrowheads) in the Δ*cisA* mutant, whereas in ghost cells derived
592 from the WT and the complemented mutant, CIS^{Sc} particles (black arrowheads) are mostly
593 contracted. See also Supplementary Fig. 1. PG, peptidoglycan; CM, cytoplasmic membrane;
594 Bars, 50 nm.

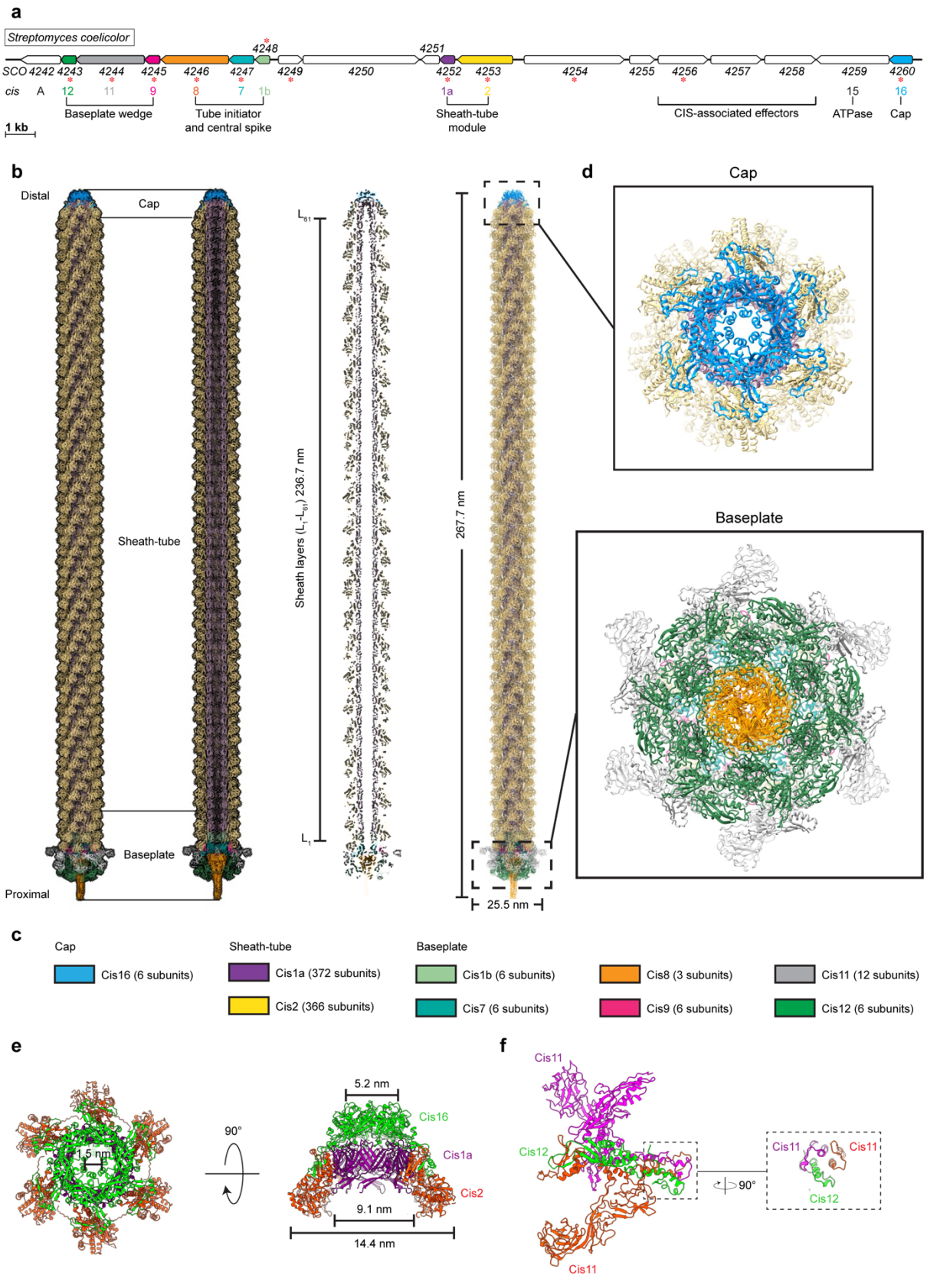
a
Streptomyces coelicolor
SCO 4242 4243 4244 4245 4246 4247 4248 4249 4250 4251 4252 4253 4254 4255 4256 4257 4258 4259 4260
cis A 12 11 9 8 7 1b 1a 2 15 16
Baseplate wedge
Tube initiator and central spike
Sheath-tube module
CIS-associated effectors
ATPase
Cap
1 kb
b
Distal
Cap
Sheath-tube
Baseplate
Proximal
Sheath layers (L1-L61) 236.7 nm
267.7 nm
25.5 nm
d
Cap
Baseplate
c
Cap
Cis16 (6 subunits)
Sheath-tube
Cis1a (372 subunits)
Cis2 (366 subunits)
Baseplate
Cis1b (6 subunits)
Cis7 (6 subunits)
Cis8 (3 subunits)
Cis9 (6 subunits)
Cis11 (12 subunits)
Cis12 (6 subunits)
e
1.5 nm
90°
5.2 nm
Cis16
Cis1a
Cis2
9.1 nm
14.4 nm
f
Cis11
Cis12
90°

595

596

597 **Figure 2: CryoEM structure of the extended CIS^{Sc} assembly reveals its composition.**

598 **a.** Schematic illustrating the CIS^{Sc} gene cluster (adapted from (18)). Asterisks indicate gene
599 products that were detected by mass spectrometry analyzing crude preparations of CIS^{Sc}
600 particles (red). See also Supplementary Table 1.

601 **b/c.** Single-particle cryoEM structure of an extended CIS^{Sc} assembly obtained purified from a
602 non-contractile CIS^{Sc} mutant. Shown are the composite atomic model in surface (left) and
603 ribbon (right) rendering (b). Subunits are color-coded according to (a) and their copy numbers
604 in the assembly are indicated in (c).

605 **d.** Perpendicular views of the ribbon representation of the CIS^{Sc} model of the cap and baseplate
606 modules.

607 **e.** Top view (left) and side view (right) of ribbon diagrams showing the cap module of CIS^{Sc},
608 revealing that the cap is composed of a Cis16 hexamer.

609 **f.** Ribbon diagrams showing a single baseplate wedge subunit, which is composed of two
610 copies of Cis11 and one copy of Cis12.

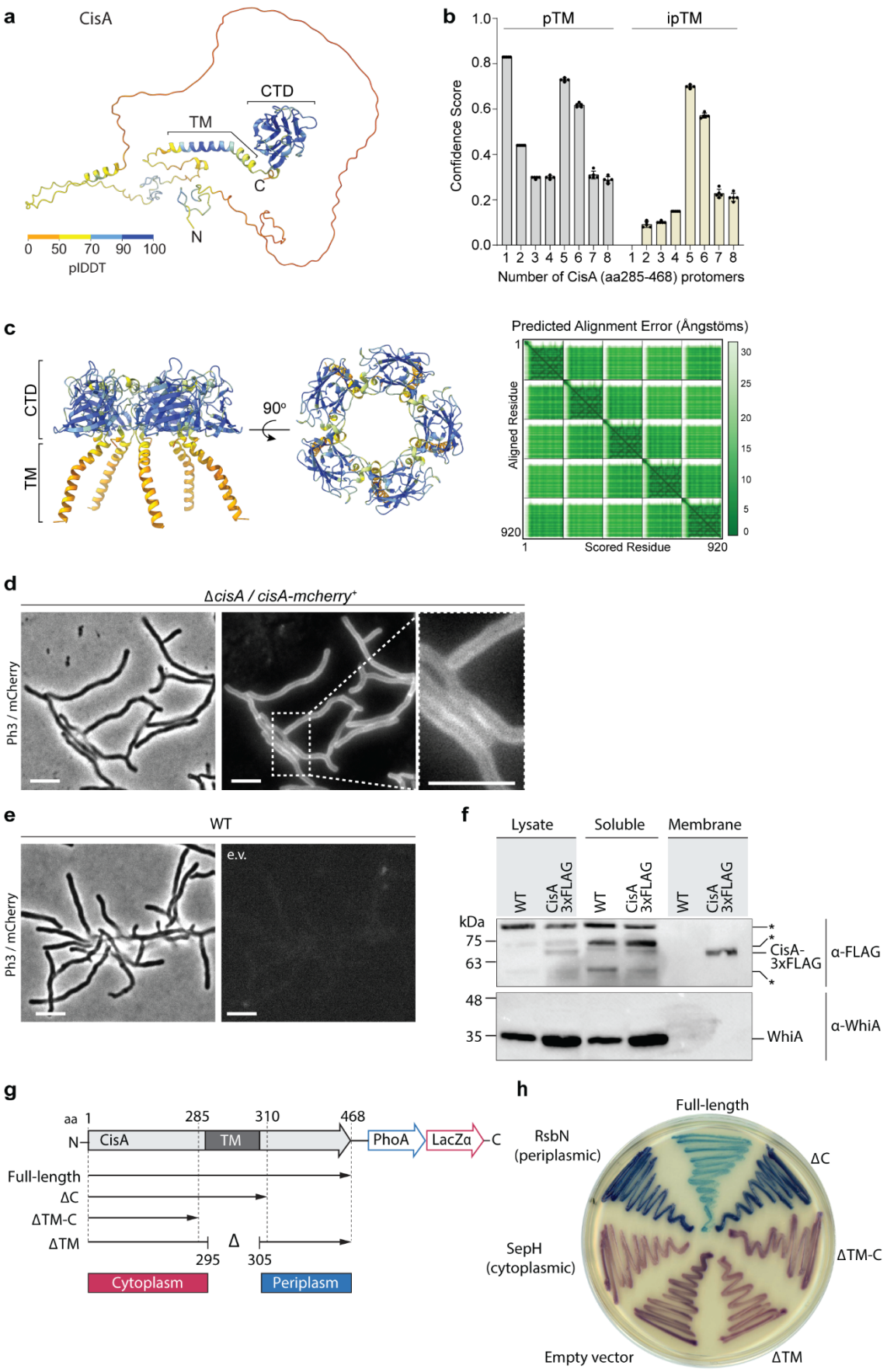
a
CisA
CTD
TM
C
N
0 50 70 90 100
pIDDT
b
pTM
ipTM
Confidence Score
1.0
0.8
0.6
0.4
0.2
0.0
1 2 3 4 5 6 7 8 1 2 3 4 5 6 7 8
Number of CisA (aa285-468) protomers
c
CTD
TM
90°
Predicted Alignment Error (Ångstöms)
Aligned Residue
Scored Residue
1
920
30
25
20
15
10
5
0
d
ΔcisA / cisA-mcherry+
Ph3 / mCherry
e
WT
Ph3 / mCherry
e.v.
f
Lysate
Soluble
Membrane
WT
CisA 3xFLAG
kDa
75
63
48
35
CisA-3xFLAG
α-FLAG
WhiA
α-WhiA
g
aa 1
285
310
468
N
CisA
TM
PhoA
LacZα
C
Full-length
ΔC
ΔTM-C
ΔTM
Δ
295
305
Cytoplasm
Periplasm
h
Full-length
RsbN (periplasmic)
ΔC
SepH (cytoplasmic)
ΔTM-C
Empty vector
ΔTM

611

612 **Figure 3: CisA is a single-pass membrane protein predicted to oligomerize.**

613 **a.** Alphafold3 model of CisA colored in pLDDT values. CisA is predicted to contain a largely
614 unstructured N-terminal domain, a transmembrane domain (TM) and a conserved C-terminal
615 (CTD).

616 **b.** Confidence scores for the predicted oligomeric configuration of CisA. Shown are the
617 predicted template modeling (pTM) and the predicted interface pTM scores (ipTM) obtained
618 from n = 5 predictions per CisA configuration. An ipTM score greater than 0.7 indicates a
619 likely protein–protein interaction. CisA aa 285-468, including the transmembrane domain and
620 the CTD (amino acid 285-468), was used as input sequences for modeling.

621 **c.** Alphafold3 model of a CisA (amino acids 285-468) pentamer and the corresponding
622 predicted alignment error (PAE) plot.

623 **d/e.** Representative micrographs (left panels: phase contrast, Ph3; right panel: mCherry) of
624 strains of *S. coelicolor* vegetative hyphae either constitutively expressing CisA-mCherry
625 (Δ*cisA/cisA-mcherry*) *in trans* (d) or WT cells carrying an empty vector (e.v.) to control for
626 background fluorescence (e). Box shows a magnified region of hyphae with CisA-mCherry
627 accumulation in the cellular periphery. Bars, 5 µm.

628 **f.** Western blot of the cellular fractionation of samples from the *S. coelicolor* WT or the Δ*cisA*
629 mutant constitutively expressing a CisA-3xFLAG fusion *in trans*. Lysate and soluble and
630 membrane fractions were probed for the presence of CisA-3xFLAG with an α-FLAG antibody
631 (top). Fractionation efficiency was assessed using an α-WhiA antibody to detect the soluble
632 transcription factor WhiA (bottom). The same volumes for each fraction were loaded and
633 analyzed by immunoblotting. CisA-3xFLAG was detected in the lysate and the membrane
634 fraction. Asterisks denote non-specific signals. The experiment was performed in biological
635 duplicates and shown is a representative image.

636 **g/h.** Experimental determination of the CisA membrane topology using the dual *phoA-lacZα*
637 reporter in *E. coli*. The schematic diagram (g) depicts the four CisA constructs used in the assay
638 and indicates the relevant amino acid (aa) deleted in the three CisA mutant derivates. The
639 analysis of colony coloration (h); pink coloration for cytosolic proteins and blue coloration for
640 periplasmic proteins, indicates that the CisA N-terminus is localized in the cytoplasm and the

641 CisA C-terminus localized to the periplasm and this topology is dependent on the
642 transmembrane domain (TM). *E. coli* strains carrying an empty reporter plasmid or reporter
643 plasmids with the *Streptomyces* genes for SepH (cytoplasmic) and RsbN (periplasmic) were
644 used as controls. Note that the expression of full-length CisA in *E. coli* is toxic, resulting in
645 reduced growth and a lighter blue coloration.

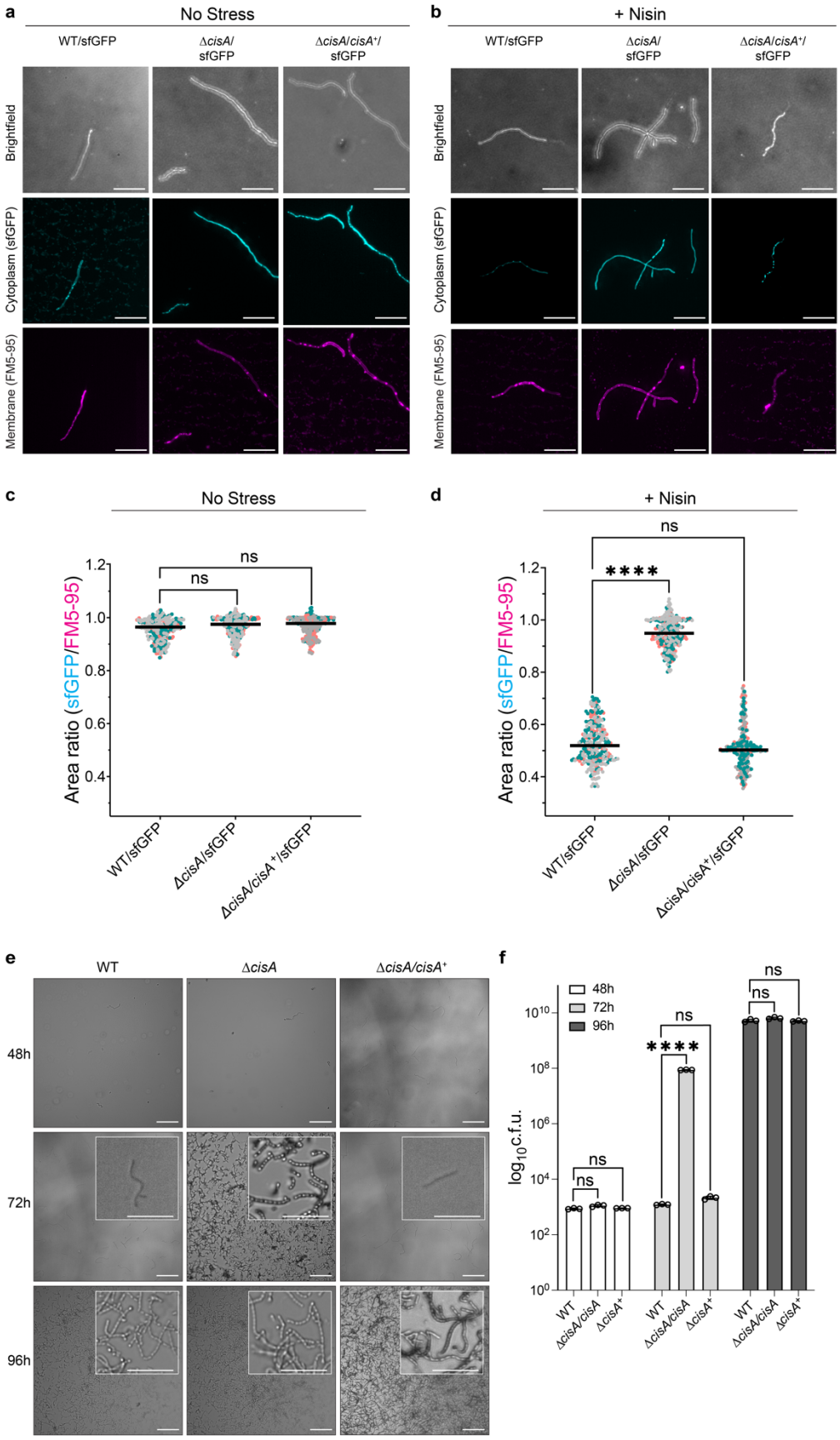
a
No Stress
WT/sfGFP
ΔcisA/ sfGFP
ΔcisA/cisA+/ sfGFP
Brightfield
Cytoplasm (sfGFP)
Membrane (FM5-95)
b
+ Nisin
c
Area ratio (sfGFP/FM5-95)
ns
d
****
e
WT
ΔcisA
ΔcisA/cisA+
48h
72h
96h
f
log10c.f.u.
ns
****

647 **Figure 4: CisA is required for regulated cell death and cellular function of CIS^{Sc}.**

648 **a-d.** Light microscopy-based viability assay showing that CIS^{Sc} do not mediate cell death in
649 *cisA*-deficient hyphae in response to exogenous stress. Shown are representative micrographs
650 of the WT/sfGFP, the Δ*cisA*/sfGFP and the complemented Δ*cisA/cisA*$^{+}$/sfGFP mutant
651 expressing cytosolic sfGFP (indicator for live cells). Strains were grown for 48 h and then
652 either incubated without (a) or with (b) the membrane-disrupting antibiotic nisin (1 µg/ml nisin
653 for 90 min). Samples were briefly vortexed to break up mycelial clumps and subsequently
654 stained with the fluorescent membrane dye FM5-95 to stain cells with an intact or damaged
655 cytoplasmic membrane. Bars, 10 µm. Z-stacks were taken of the samples, and the resulting
656 relative fluorescence ratios of sfGFP to FM5-95 are shown in c/d. WT and Δ*cisA/cisA*$^{+}$
657 complemented cells showed a significantly higher rate of cell death in response to nisin
658 treatment than Δ*cisA* cells. There is no significant difference in the viability of the tested strains
659 in the absence of nisin. Experiments were performed in three biological replicates, as indicated
660 by the green, grey, and magenta data points. Black lines indicate the mean ratio derived from
661 biological triplicate experiments (n=100 images per replicate). ns (not significant) and ****
662 ($p < 0.0001$) were determined using a one-way ANOVA and Tukey's post-test.

663 **e.** Visualization of spore production in WT, Δ*cisA* mutant and Δ*cisA/cisA*$^{+}$ strains reveal
664 accelerated cellular development and sporulation of the Δ*cisA* mutant. Shown are
665 representative brightfield images of surface impressions of plate-grown colonies of each strain
666 taken at the indicated time points. Only sporulating hyphae will attach to the hydrophobic cover
667 glass surface. Insets show magnified regions of the colony surface containing spores and spore
668 chains. Bars, 50 µm.

669 **f.** Quantification of sporulation shown in (e) via counts of colony-forming units (c.f.u.). The
670 graph shows a 6-fold higher c.f.u. count at 72 h in the Δ*cisA* mutant. Strains were grown on
671 R2YE agar and spores were harvested after 48 h, 72 h, and 96 h of incubation. Data show mean
672 ± s.d. obtained from biological triplicate experiments. ns (not significant) and ****
673 ($p < 0.0001$) were determined using a one-way ANOVA and Tukey's post-test.

674

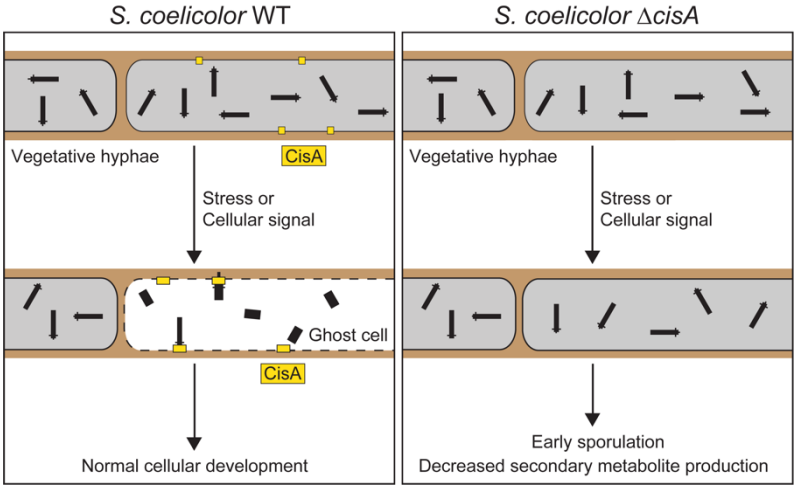

675 **Figure 5: Cytoplasmic CIS^{Sc} require the membrane protein CisA for contraction and**
676 **function.**

677 Proposed model illustrating a possible role of CisA. In response to exogenous stress or an
678 unknown cellular signal, membrane-bound CisA either directly or indirectly mediates the
679 association of free-floating CIS^{Sc} particles with the cytoplasmic membrane, leading to CIS^{Sc}
680 firing and regulated cell death, which impacts the *Streptomyces* developmental life cycle.
681

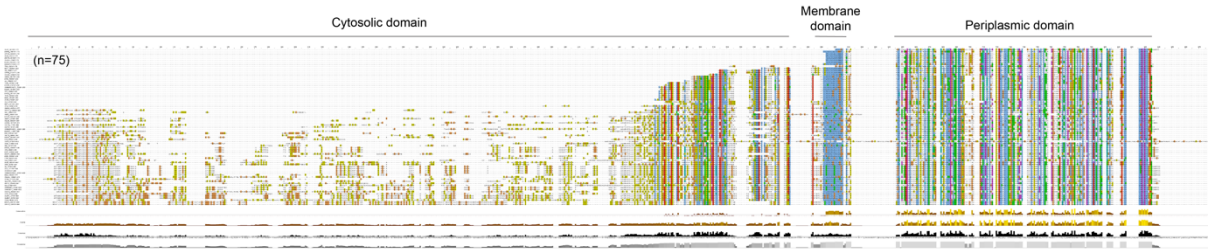

Supplementary Figure 1: CisA is conserved among CIS-positive *Streptomyces* and Actinomycete species.

Protein alignment of CisA homologs identified via reciprocal BLAST search in genomes of *Streptomyces* and actinomycete species previously reported to encode an eCIS class IId region. Protein sequences (n=75) were aligned with Clustal Omega and visualized using JalView. CisA domain structure is indicated on top. Genome accession numbers and BLAST results are listed in Supplementary Data 1 and 2.

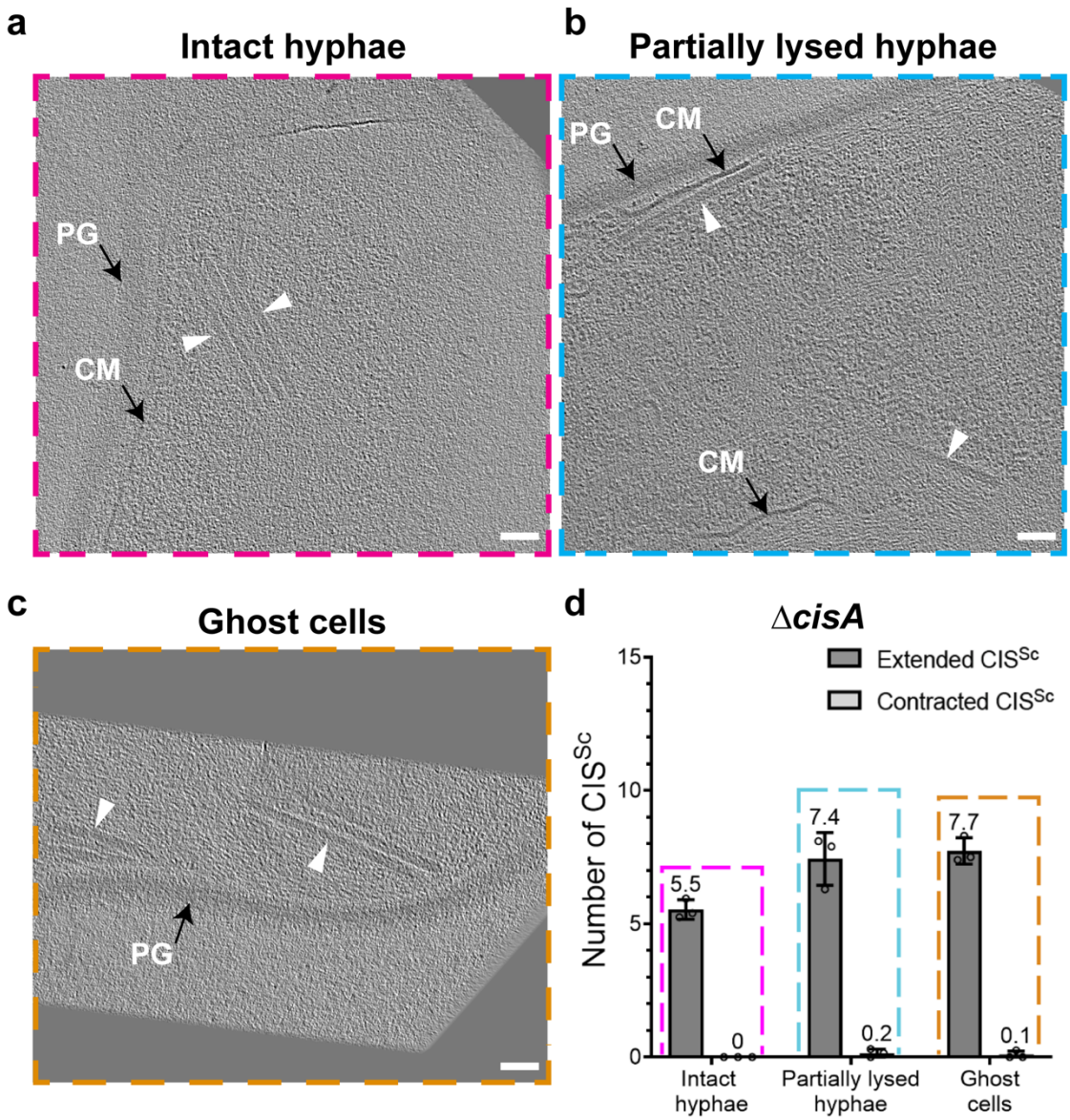

Supplementary Figure 2: Sheath contraction *in situ* is linked to the presence of CisA.

a-c. Shown are additional cryo-tomographic slices (thickness 11 nm) of *S. coelicolor* Δ*cisA* vegetative hyphae, which were observed as 'Intact hyphae' (a), 'Partially lysed hyphae' (b) and 'Ghost cells' (c). Note that all visible CIS^{Sc} particles (white arrowheads) are in the extended conformation. PG, peptidoglycan; CM, cytoplasmic membrane/membranes. Bars, 50 nm.

d. Shown is a quantification of CIS^{Sc} assemblies per tomogram and their conformations as observed in different classes of Δ*cisA* hyphae. Almost all CIS^{Sc} particles were seen in the extended conformation, indicating that sheath contraction *in situ* correlates with the presence of CisA. Data shows mean values and standard deviations obtained from biological triplicate experiments, with n=30 tomograms for each class of hyphae.

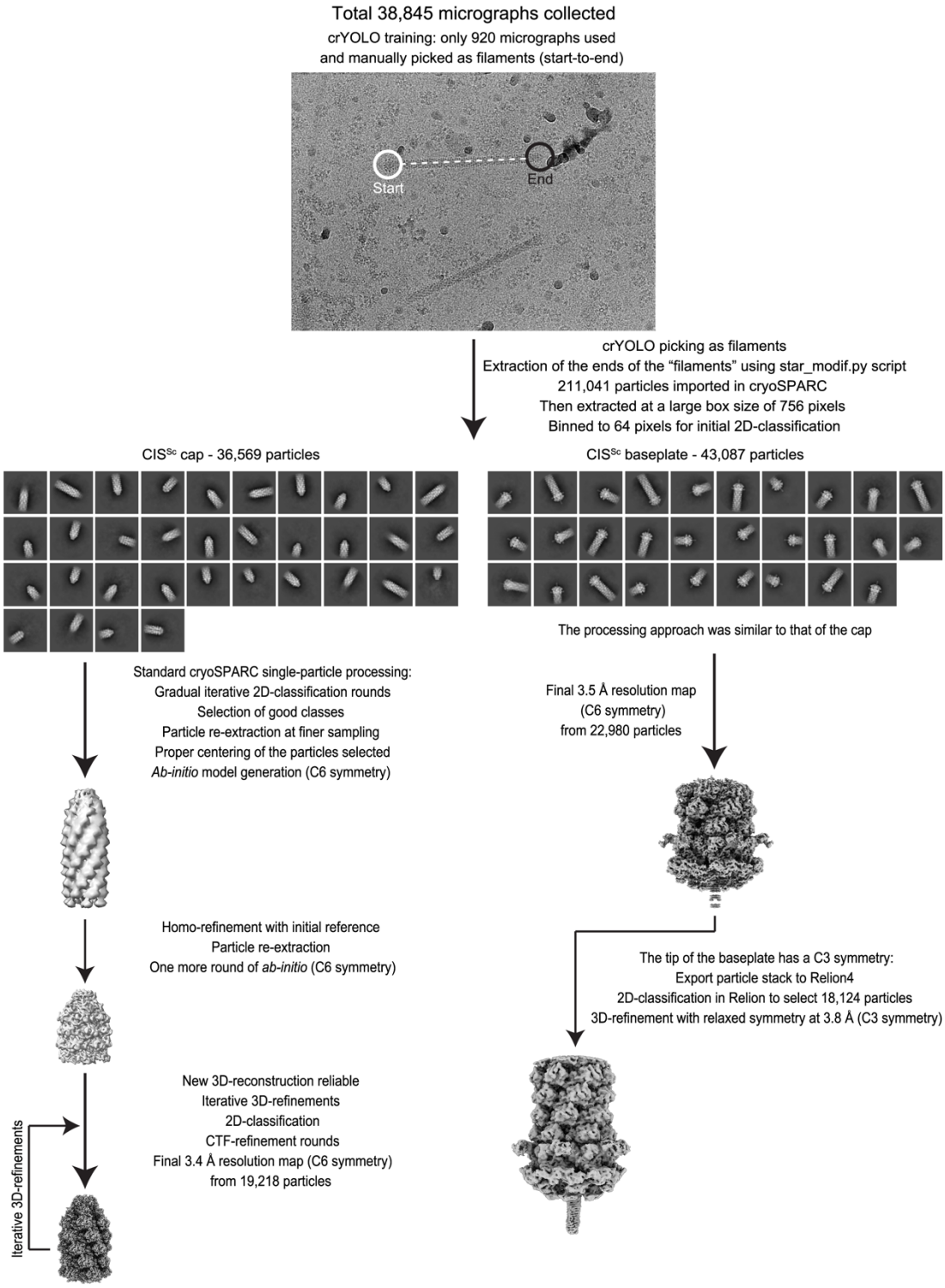

Supplementary Figure 3: Workflow for the cryoEM structural determination of the extended CIS^{Sc}.

Flowchart for cryoEM reconstruction of the extended CIS^{Sc} particle. See METHODS and Supplementary Table 1 for details.

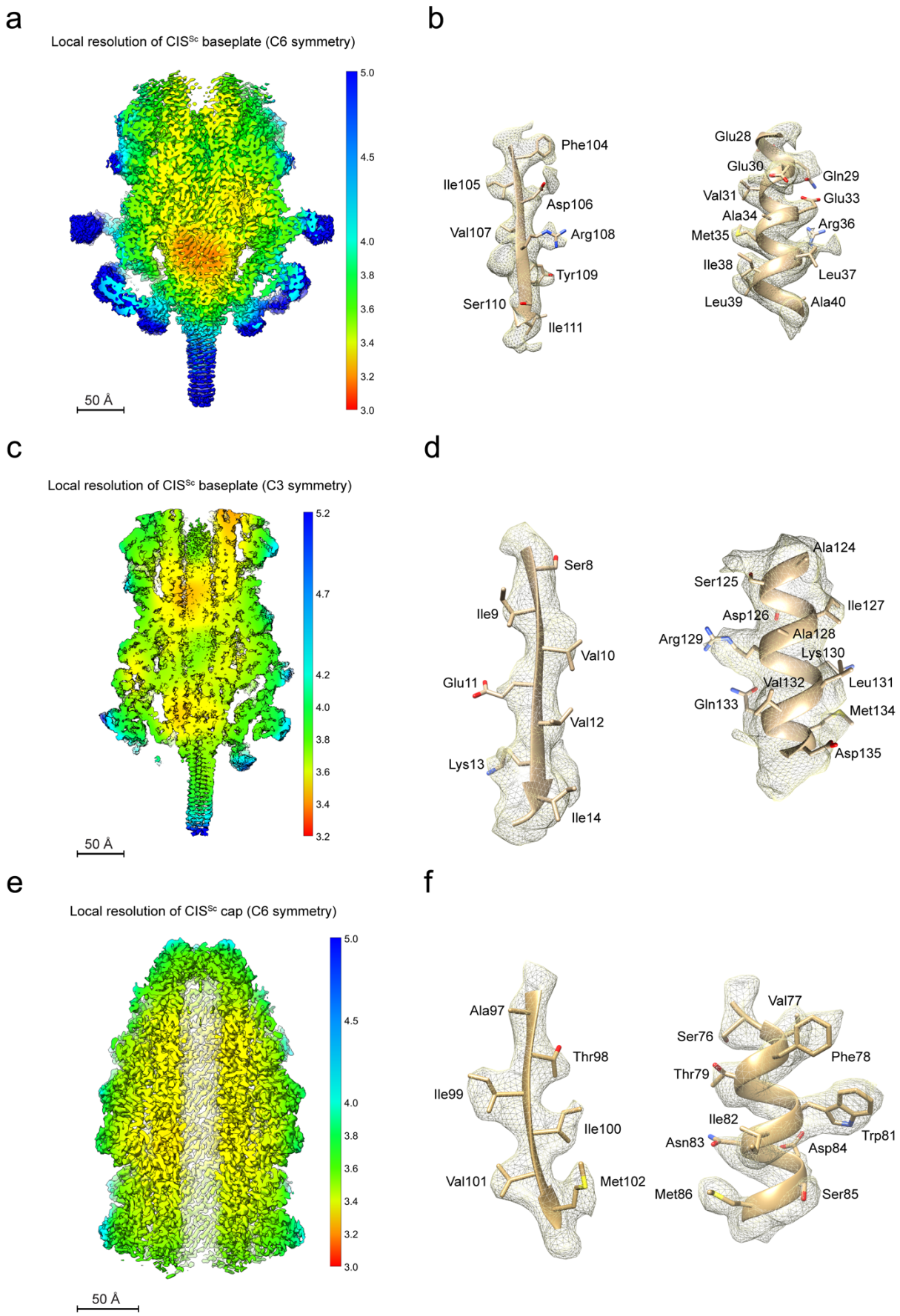
a
Local resolution of CIS^Sc baseplate (C6 symmetry)
5.0
4.5
4.0
3.8
3.6
3.4
3.2
3.0
50 Å
b
Phe104
Ile105
Asp106
Val107
Arg108
Tyr109
Ser110
Ile111
Glu28
Glu30
Gln29
Val31
Glu33
Ala34
Arg36
Met35
Ile38
Leu37
Leu39
Ala40
c
Local resolution of CIS^Sc baseplate (C3 symmetry)
5.2
4.7
4.2
4.0
3.8
3.6
3.4
3.2
50 Å
d
Ser8
Ile9
Val10
Glu11
Val12
Lys13
Ile14
Ala124
Ser125
Ile127
Asp126
Arg129
Ala128
Lys130
Leu131
Val132
Gln133
Met134
Asp135
e
Local resolution of CIS^Sc cap (C6 symmetry)
5.0
4.5
4.0
3.8
3.6
3.4
3.2
3.0
50 Å
f
Ala97
Thr98
Ile99
Ile100
Val101
Met102
Val77
Ser76
Phe78
Thr79
Ile82
Trp81
Asn83
Asp84
Met86
Ser85

707

708

709 **Supplementary Figure 4: Map qualities of different CIS^{Sc} modules.**

710 **a-f.** Local resolution maps of the CIS^{Sc} baseplate with C6 symmetry (a), CIS^{Sc} baseplate with
711 C3 symmetry (c), and the CIS^{Sc} cap with C6 symmetry (e). (d-f) shows regions of the cryoEM
712 density map (mesh) that were superimposed with the atomic models (ribbons and sticks),
713 demonstrating the agreement between the observed and modeled amino acid side chains for
714 one beta-sheet (left) and one alpha helix (right). Shown are examples of the baseplate with C6
715 symmetry (b), the baseplate with C3 symmetry (d), and the cap with C6 symmetry (f).

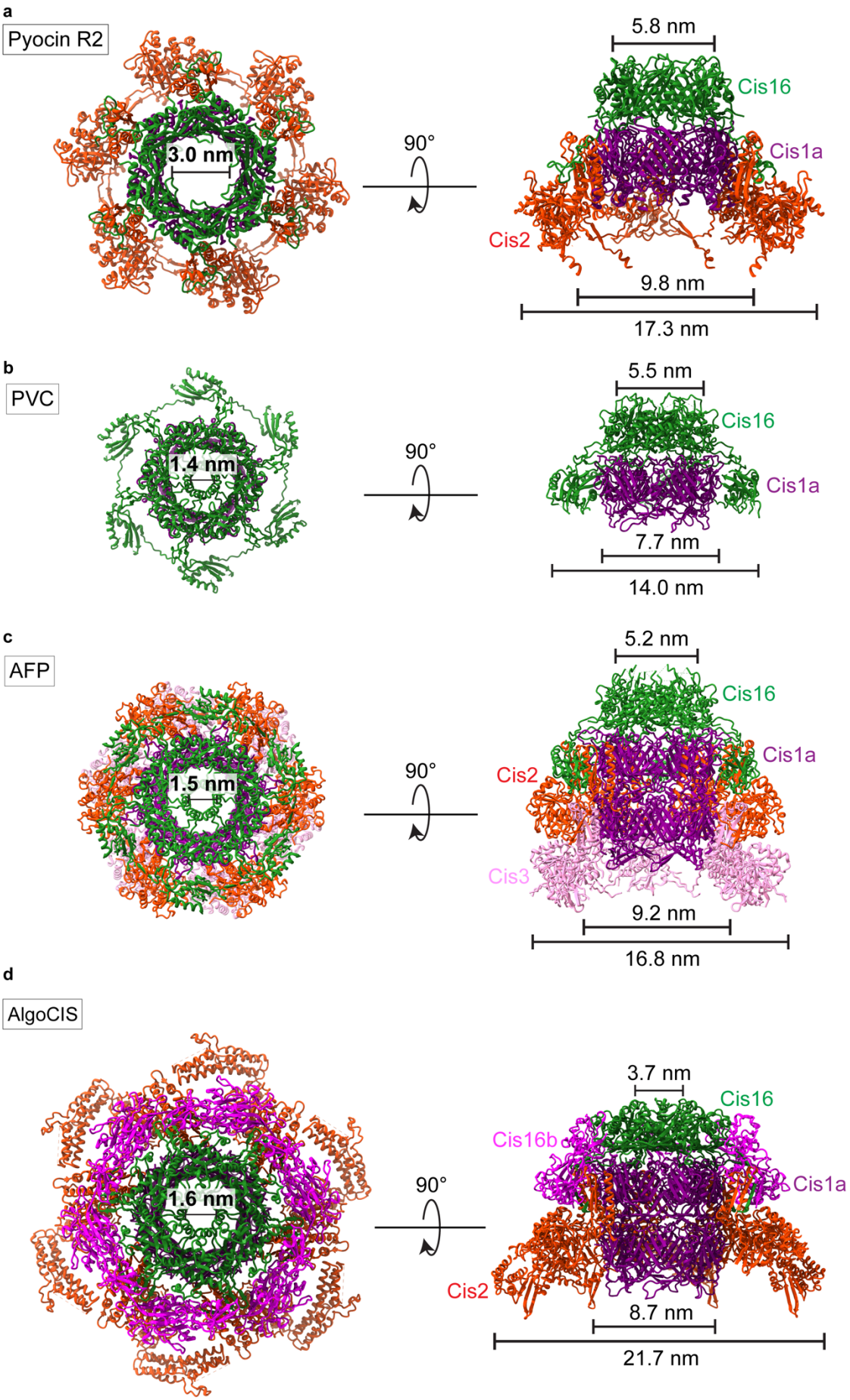
a
Pyocin R2
3.0 nm
90°
5.8 nm
Cis16
Cis1a
Cis2
9.8 nm
17.3 nm
b
PVC
1.4 nm
90°
5.5 nm
Cis16
Cis1a
7.7 nm
14.0 nm
c
AFP
1.5 nm
90°
5.2 nm
Cis16
Cis1a
Cis2
Cis3
9.2 nm
16.8 nm
d
AlgoCIS
1.6 nm
90°
3.7 nm
Cis16
Cis16b
Cis1a
Cis2
8.7 nm
21.7 nm

716

717 **Supplementary Figure 5: Structures of the cap modules of other CISs**.

718 **a-d.** Top views (left) and side views (right) of ribbon representations of the structures of CIS
719 cap modules of Pyocin R2 (a, PDB 6U5B), PVC (b, PDB 6J0N), AFP (**c**, PDB 6RAP) and
720 AlgoCIS (d, PDB 7ADZ).

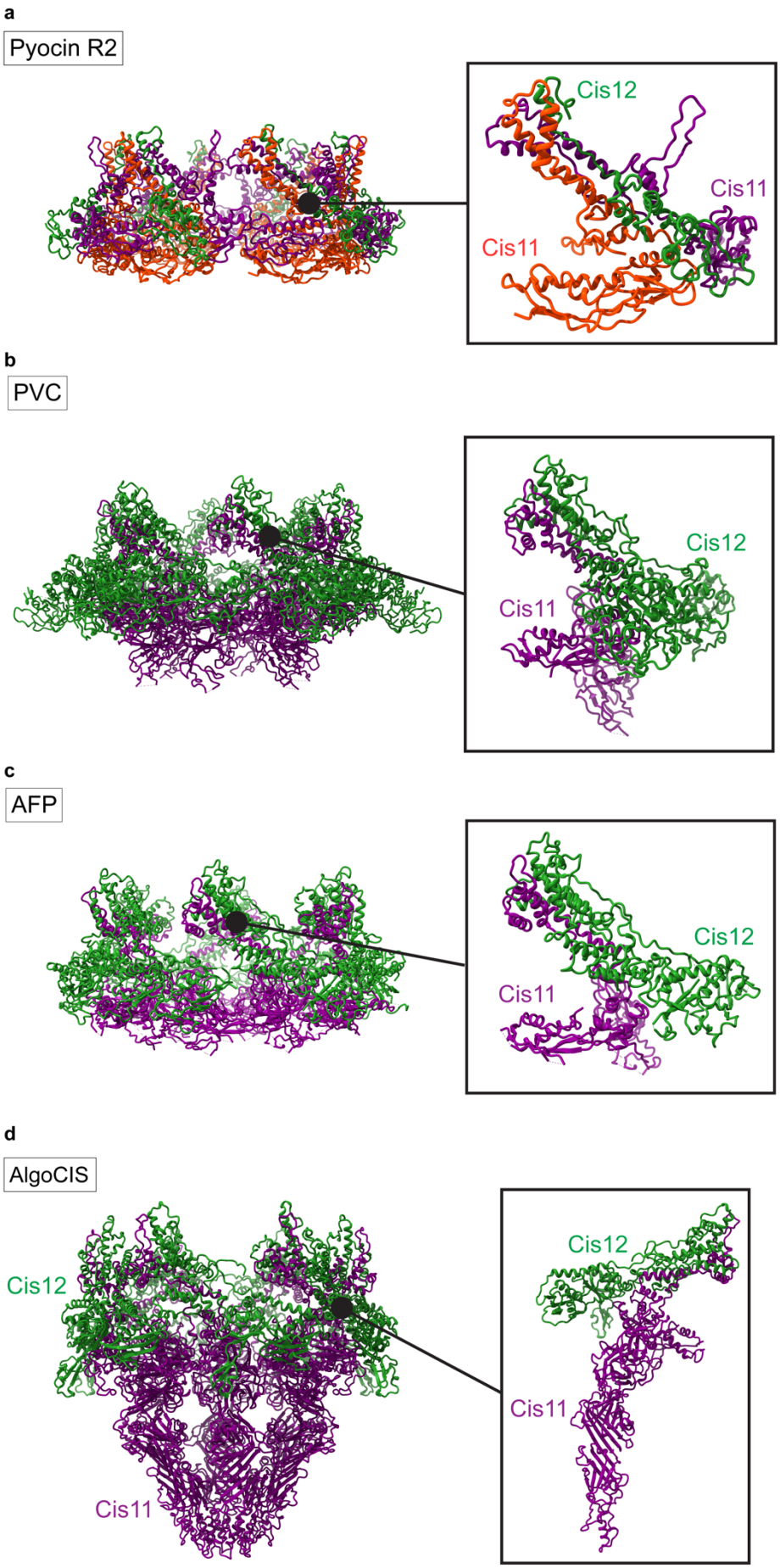
a
Pyocin R2
Cis12
Cis11
Cis11
b
PVC
Cis12
Cis11
c
AFP
Cis12
Cis11
d
AlgoCIS
Cis12
Cis11
Cis12
Cis11

721

722 **Supplementary Figure 6: Structures of the baseplate modules of other CISs**.

723 **a-d.** Ribbon representations of the full structures (left) and the individual wedge subunit (right)
724 of the CIS baseplate components (Cis11/12) of Pyocin R2 (a, PDB 6U5F), PVC (b, PDB 6J0F),
725 AFP (c, PDB 6RAO) and AlgoCIS (d, PDB 7AEB).

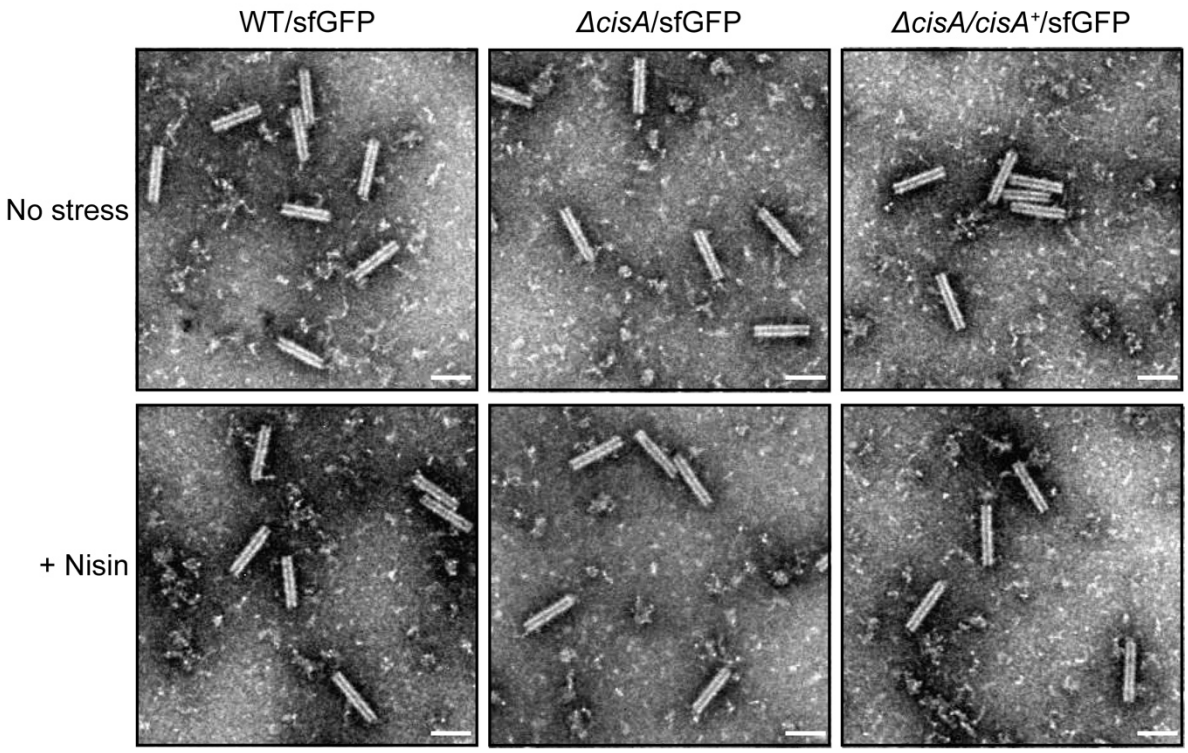

726

727 **Supplementary Figure 7: Control experiment showing that the behavior of purified CIS^{Sc}**
728 **particles is wild-type-like in the strains used in the viability assay.**

729 Representative negative-stain electron micrographs of purified CIS^{Sc} particles from the
730 WT/sfGFP, the Δ*cisA*/sfGFP mutant and the Δ*cisA*/Δ*cisA*$^{+}$/sfGFP complemented mutant
731 exposed to no stress (upper row) or 1 µg/ml nisin (lower row). No differences were observed
732 between the overall structure of CIS^{Sc} particles. These experiments were performed three
733 independent times. Bars, 100 nm.

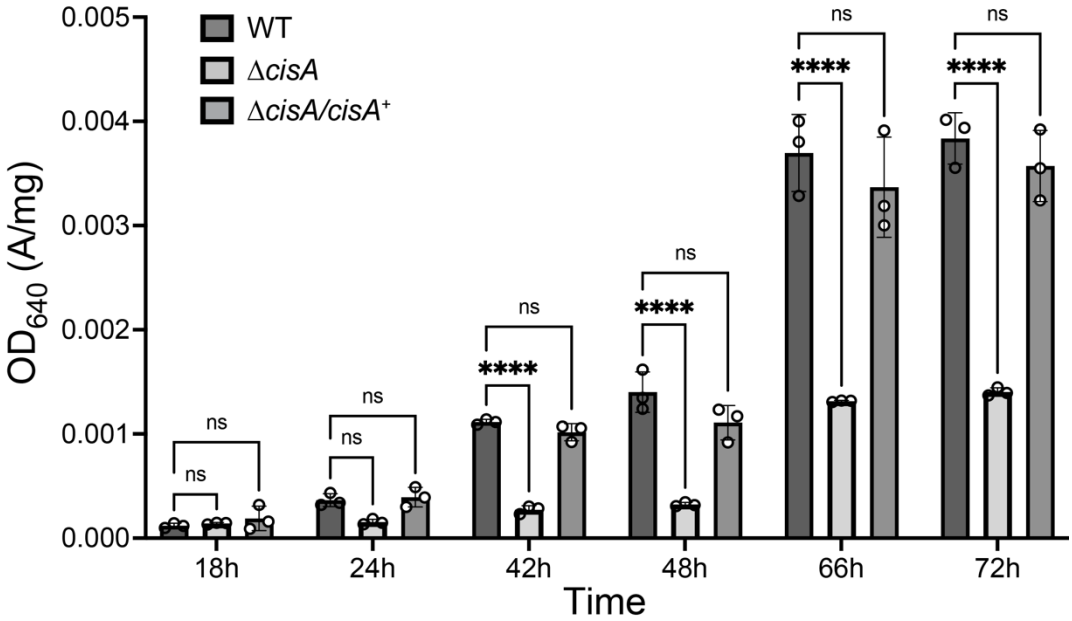

734

735 **Supplementary Figure 8: CisA impacts secondary metabolite production.**

736 Quantification of total actinorhodin production by the WT, the Δ*cisA* mutant and the
737 complemented Δ*cis*A/Δ*cisA*$^{+}$ mutant grown in R2YE medium, revealing reduced actinorhodin
738 production in the Δ*cisA* mutant. Samples were taken at the indicated time points. Actinorhodin
739 was extracted and quantified by measuring the optical density OD_{640} of the culture supernatant
740 (65) and normalized to the wet cell pellet weight. Analysis was performed in biological
741 triplicate experiments. The mean values and standard error are shown. ns (not significant) and
742 **** ($p < 0.0001$) were calculated using one-way ANOVA and Tukey's post-test.

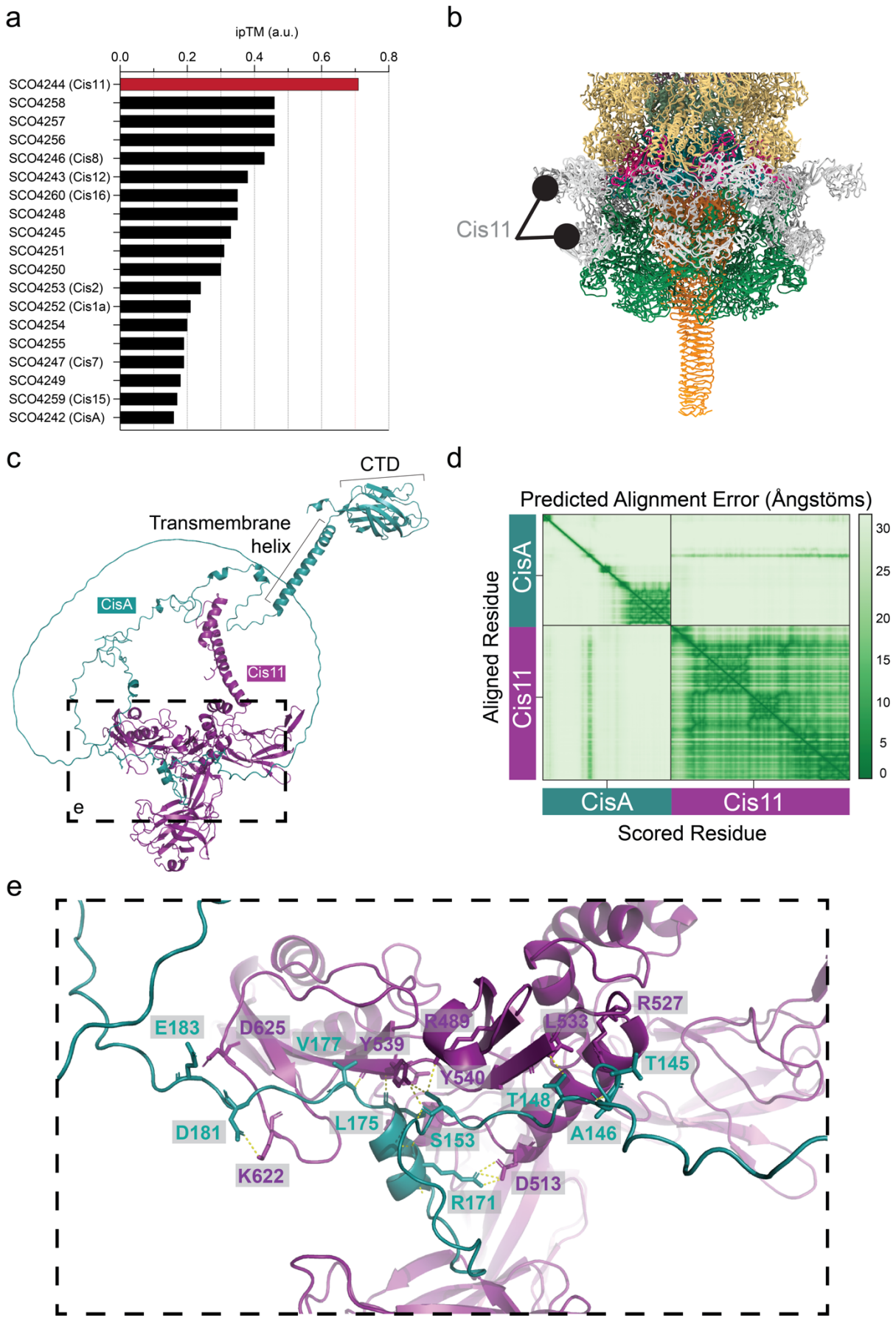
a
ipTM (a.u.)
0.0
0.2
0.4
0.6
0.8
SCO4244 (Cis11)
SCO4258
SCO4257
SCO4256
SCO4246 (Cis8)
SCO4243 (Cis12)
SCO4260 (Cis16)
SCO4248
SCO4245
SCO4251
SCO4250
SCO4253 (Cis2)
SCO4252 (Cis1a)
SCO4254
SCO4255
SCO4247 (Cis7)
SCO4249
SCO4259 (Cis15)
SCO4242 (CisA)
b
Cis11
c
CTD
Transmembrane helix
CisA
Cis11
e
d
Predicted Alignment Error (Ångstöms)
Aligned Residue
CisA
Cis11
Scored Residue
30
25
20
15
10
5
0
e
E183
D625
V177
Y539
R489
L533
R527
T145
Y540
T148
A146
D181
L175
S153
K622
D513
R171

744 **Supplementary Figure 9: *In silico* protein-protein interaction analyses predict that CisA**
745 **binds a CIS^{Sc} baseplate component.**
746 **a.** An AlphaFold2-Multimer-based protein-protein interaction screen between monomeric
747 CisA and the 19 gene products of the CIS^{Sc} gene cluster suggests an interaction between CisA
748 and the baseplate component Cis11. The likelihood of a protein-protein interaction was ranked
749 based on the interface pTM (ipTM) confidence score, with an ipTM greater than 0.7 indicating
750 a potential protein-protein interaction.
751 **b.** Zoomed-in view of the SPA-cryoEM structure of the CIS^{Sc} baseplate complex (Fig. 2b/d),
752 illustrating the peripheral and surface-exposed position of Cis11.
753 **c.** The Alphafold3 model of the CisA-Cis11 complex. The conserved C-terminal domain
754 (CTD) of CisA is located in the periplasm.
755 **d.** The Alphafold3 predicted aligned error (%) heatmap plot of the concatenated Cis11 and
756 CisA input sequence.
757 **e.** Zoomed-in view of the relevant side chains at the CisA-Cis11 interface.

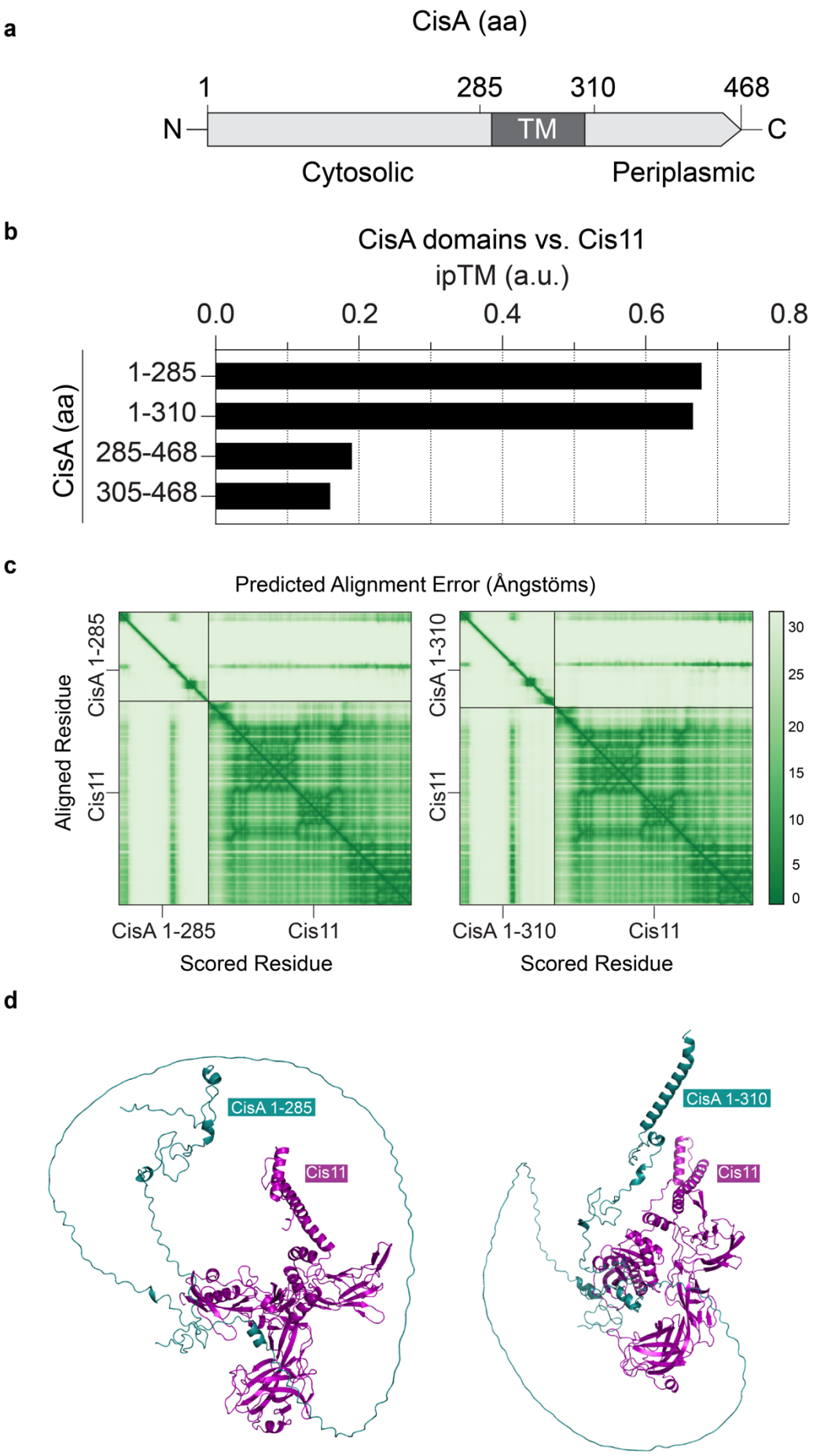
a
CisA (aa)
1
285
310
468
N
TM
C
Cytosolic
Periplasmic
b
CisA domains vs. Cis11
ipTM (a.u.)
0.0
0.2
0.4
0.6
0.8
CisA (aa)
1-285
1-310
285-468
305-468
c
Predicted Alignment Error (Ångstöms)
Aligned Residue
CisA 1-285
Cis11
CisA 1-310
Cis11
30
25
20
15
10
5
0
CisA 1-285
Cis11
Scored Residue
CisA 1-310
Cis11
Scored Residue
d
CisA 1-285
Cis11
CisA 1-310
Cis11

758

759 **Supplementary Figure 10: The cytosolic part of CisA is predicted to interact with Cis11.**

760 **a.** Schematic showing the CisA domain organization. Relevant amino acid (aa) positions are
761 shown above. TM, transmembrane domain.
762 **b.** AlphaFold2-Multimer based protein-protein interaction screen between monomers of CisA
763 and truncated versions of CisA and Cis11. The likelihood of a protein-protein interaction was
764 ranked based on the interface pTM (ipTM) confidence score.
765 **c/d.** Predicted CisA-Cis11 complexes using truncated versions of CisA (amino acids 1-285 and
766 1-310) show that the largely unstructured cytosolic portion of CisA is required to interact with
767 Cis11. (c) The Alphafold3 predicted aligned error (%) heatmap plots of the concatenated Cis11
768 and truncated CisA 1-285 and CisA 1-310 input sequences. (d) The Alphafold3 model of the
769 CisA 1-285-Cis11 (left) and CisA 1-310-Cis11 (right) complexes.

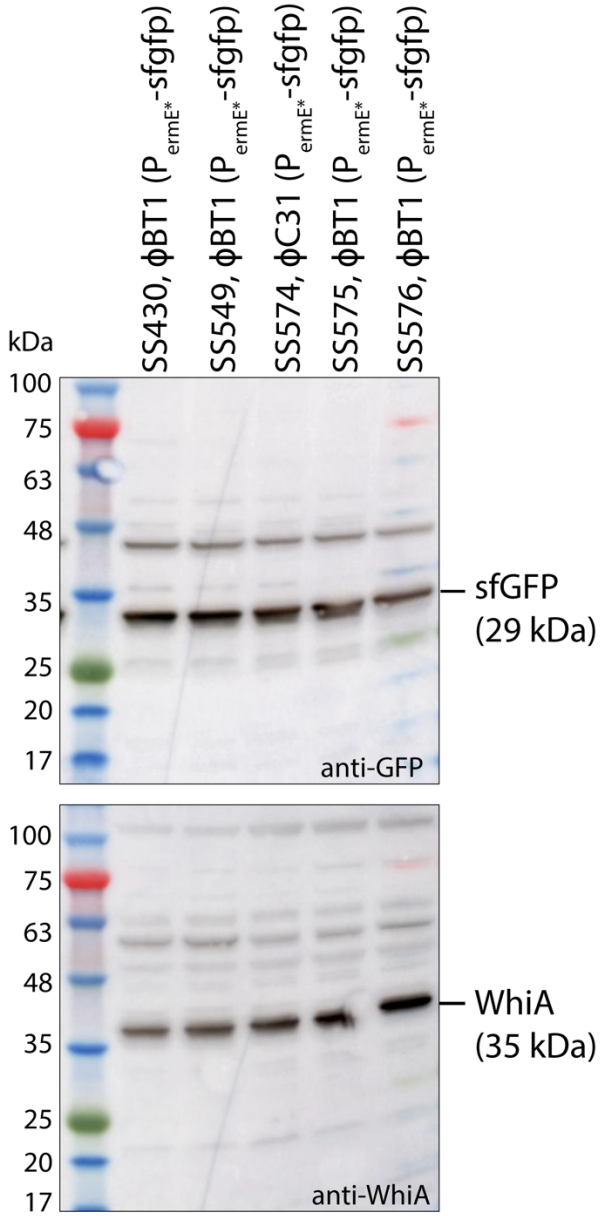

Supplementary Figure 11: Western blot confirming similar levels of cytosolic sfGFP in strains used for viability assays.

Control experiments to verify similar protein levels of sfGFP, which was expressed either from the ϕC31 or the ϕBT1 phage attachment site in the *S. coelicolor* genome. The expression of sfgfp was driven by the constitutive *ermE** promoter (P_{ermE*}). Equal amounts of total protein were loaded and sfGFP levels were detected with an anti-GFP antibody. As a control, the same cell lysates were also probed with an anti-WhiA antibody. Shown are representative results of duplicate experiments.

References

1. Lin L. The expanding universe of contractile injection systems in bacteria. Curr Opin Microbiol. 2024 Jun 1;79:102465.

2. Brackmann M, Nazarov S, Wang J, Basler M. Using Force to Punch Holes: Mechanics of Contractile Nanomachines. Trends Cell Biol. 2017 Sep;27(9):623–32.

3. Taylor NMI, van Raaij MJ, Leiman PG. Contractile injection systems of bacteriophages and related systems. Mol Microbiol. 2018 Apr;108(1):6–15.

4. Taylor NMI, Prokhorov NS, Guerrero-Ferreira RC, Shneider MM, Browning C, Goldie KN, et al. Structure of the T4 baseplate and its function in triggering sheath contraction. Nature. 2016 May 19;533(7603):346–52.

5. Böck D, Medeiros JM, Tsao HF, Penz T, Weiss GL, Aistleitner K, et al. *In situ* architecture, function, and evolution of a contractile injection system. Science. 2017 Aug 18;357(6352):713–7.

6. Allsopp LP, Bernal P. Killing in the name of: T6SS structure and effector diversity. Microbiology. 2023;169(7):001367.

7. Coulthurst S. The Type VI secretion system: a versatile bacterial weapon. Microbiology (Reading). 2019 May;165(5):503-515.

8. Chen L, Song N, Liu B, Zhang N, Alikhan NF, Zhou Z, et al. Genome-wide Identification and Characterization of a Superfamily of Bacterial Extracellular Contractile Injection Systems. Cell Rep. 2019 Oct 8;29(2):511-521.e2.

9. Geller AM, Pollin I, Zlotkin D, Danov A, Nachmias N, Andreopoulos WB, et al. The extracellular contractile injection system is enriched in environmental microbes and associates with numerous toxins. Nat Commun. 2021 Jun 18;12(1):3743.

10. Basler M, Pilhofer M, Henderson GP, Jensen GJ, Mekalanos JJ. Type VI secretion requires a dynamic contractile phage tail-like structure. Nature. 2012 Feb 26;483(7388):182–6.

11. Durand E, Nguyen VS, Zoued A, Logger L, Péhau-Arnaudet G, Aschtgen MS, et al. Biogenesis and structure of a type VI secretion membrane core complex. Nature. 2015 Jul;523(7562):555–60.

12. Zachs T, Malit JJL, Xu J, Schürch A, Sivabalasarma S, Nußbaum P, et al. Archaeal type six secretion system mediates contact-dependent antagonism. Sci Adv. 2024 Nov 15;10(46):eadp7088.

13. Xu J, Ericson CF, Lien YW, Rutaganira FUN, Eisenstein F, Feldmüller M, et al. Identification and structure of an extracellular contractile injection system from the marine bacterium *Algoriphagus machipongonensis*. Nat Microbiol. 2022 Mar;7(3):397–410.

14. Shikuma NJ, Pilhofer M, Weiss GL, Hadfield MG, Jensen GJ, Newman DK. Marine tubeworm metamorphosis induced by arrays of bacterial phage tail-like structures. Science. 2014 Jan 31;343(6170):529–33.

816 15. Hurst MRH, Beard SS, Jackson TA, Jones SM. Isolation and characterization of the
817 *Serratia entomophila* antifeeding prophage. FEMS Microbiol Lett. 2007 May;270(1):42–
818 8.

819 16. Jiang F, Li N, Wang X, Cheng J, Huang Y, Yang Y, et al. Cryo-EM Structure and Assembly
820 of an Extracellular Contractile Injection System. Cell. 2019 Apr 4;177(2):370-383.e15.

821 17. Weiss GL, Eisenstein F, Kieninger AK, Xu J, Minas HA, Gerber M, et al. Structure of a
822 thylakoid-anchored contractile injection system in multicellular cyanobacteria. Nat
823 Microbiol. 2022 Mar;7(3):386–96.

824 18. Casu B, Sallmen JW, Schlimpert S, Pilhofer M. Cytoplasmic contractile injection systems
825 mediate cell death in *Streptomyces*. Nat Microbiol. 2023 Apr;8(4):711–26.

826 19. Vladimirov M, Zhang RX, Mak S, Nodwell JR, Davidson AR. A contractile injection
827 system is required for developmentally regulated cell death in *Streptomyces coelicolor*. Nat
828 Commun. 2023 Mar 16;14(1):1469.

829 20. Nagakubo T, Yamamoto T, Asamizu S, Toyofuku M, Nomura N, Onaka H. Phage tail-like
830 nanostructures affect microbial interactions between *Streptomyces* and fungi. Sci Rep.
831 2021 Oct 11;11:20116.

832 21. Nagakubo T, Asamizu S, Yamamoto T, Kato M, Nishiyama T, Toyofuku M, et al.
833 Intracellular Phage Tail-Like Nanostructures Affect Susceptibility of *Streptomyces*
834 *lividans* to Osmotic Stress. mSphere. 2023 Apr 11;8(3):e00114-23.

835 22. Nagakubo T, Nishiyama T, Yamamoto T, Nomura N, Toyofuku M. Contractile injection
836 systems facilitate sporogenic differentiation of *Streptomyces davawensis* through the
837 action of a phage tapemeasure protein-related effector. Nat Commun. 2024 May
838 24;15(1):4442.

839 23. Schlimpert S, Elliot MA. The Best of Both Worlds—*Streptomyces coelicolor* and
840 *Streptomyces venezuelae* as Model Species for Studying Antibiotic Production and
841 Bacterial Multicellular Development. J Bacteriol. 2023 Jun 22;205(7):e00153-23.

842 24. Flärdh K, Buttner MJ. *Streptomyces* morphogenetics: dissecting differentiation in a
843 filamentous bacterium. Nat Rev Microbiol. 2009 Jan;7(1):36–49.

844 25. Desfosses A, Venugopal H, Joshi T, Felix J, Jessop M, Jeong H, et al. Atomic structures
845 of an entire contractile injection system in both the extended and contracted states. Nat
846 Microbiol. 2019 Nov 1;4(11):1885–94.

847 26. Rybakova D, Schramm P, Mitra AK, Hurst MRH. Afp14 is involved in regulating the
848 length of Anti-feeding prophage (Afp). Mol Microbiol. 2015;96(4):815–26.

849 27. Ge P, Scholl D, Prokhorov NS, Avaylon J, Shneider MM, Browning C, et al. Action of a
850 minimal contractile bactericidal nanomachine. Nature. 2020 Apr;580(7805):658–62.

851 28. Abramson J, Adler J, Dunger J, Evans R, Green T, Pritzel A, et al. Accurate structure
852 prediction of biomolecular interactions with AlphaFold 3. Nature. 2024
853 Jun;630(8016):493–500.

29. Alexeyev MF, Winkler HH. Membrane topology of the Rickettsia prowazekii ATP/ADP translocase revealed by novel dual pho-lac reporters 1 1Edited by G. von Heijne. J Mol Biol. 1999 Jan;285(4):1503–13.

30. Ramos-León F, Bush MJ, Sallmen JW, Chandra G, Richardson J, Findlay KC, et al. A conserved cell division protein directly regulates FtsZ dynamics in filamentous and unicellular actinobacteria. eLife. 2021 Mar 17;10:e63387.

31. Bibb MJ, Domonkos A, Chandra G, Buttner MJ. Expression of the chaplin and rodlin hydrophobic sheath proteins in *Streptomyces venezuelae* is controlled by σ(BldN) and a cognate anti-sigma factor, RsbN. Mol Microbiol. 2012 Jun;84(6):1033–49.

32. Malpartida F, Hopwood DA. Molecular cloning of the whole biosynthetic pathway of a *Streptomyces* antibiotic and its expression in a heterologous host. Nature. 1984 May;309(5967):462–4.

33. Rapisarda C, Cherrak Y, Kooger R, Schmidt V, Pellarin R, Logger L, et al. *In situ* and high-resolution cryo-EM structure of a bacterial type VI secretion system membrane complex. EMBO J. 2019 May 15;38(10):e100886.

34. Lien YW, Amendola D, Lee KS, Bartlau N, Xu J, Furusawa G, et al. Mechanism of bacterial predation via ixotrophy. Science. 2024 Oct 18;386(6719):eadp0614.

35. Bongiovanni TR, Latario CJ, Le Cras Y, Trus E, Robitaille S, Swartz K, et al. Assembly of a unique membrane complex in type VI secretion systems of Bacteroidota. Nat Commun. 2024 Jan 10;15(1):429.

36. Ouyang R, Ongenae V, Muok A, Claessen D, Briegel A. Phage fibers and spikes: a nanoscale Swiss army knife for host infection. Curr Opin Microbiol. 2024 Feb 1;77:102429.

37. McLean TC. LazyAF, a pipeline for accessible medium-scale *in silico* prediction of protein-protein interactions. Microbiology (Reading). 2024 Jul;170(7):001473. doi: 10.1099/mic.0.001473.

38. van Kempen M, Kim SS, Tumescheit C, Mirdita M, Lee J, Gilchrist CLM, et al. Fast and accurate protein structure search with Foldseek. Nat Biotechnol. 2024 Feb;42(2):243–6.

39. T. Kieser M. J. Bibb M. J. Buttner K. F. Chater and D. A. Hopwood. Practical *Streptomyces* Genetics. Norwich: John Innes Foundation; 2000.

40. Gust B, Challis GL, Fowler K, Kieser T, Chater KF. PCR-targeted *Streptomyces* gene replacement identifies a protein domain needed for biosynthesis of the sesquiterpene soil odor geosmin. Proc Natl Acad Sci U S A. 2003 Feb 18;100(4):1541–6.

41. Gust B, Chandra G, Jakimowicz D, Yuqing T, Bruton CJ, Chater KF. Lambda red-mediated genetic manipulation of antibiotic-producing *Streptomyces*. Adv Appl Microbiol. 2004;54:107–28.

42. Ohi M, Li Y, Cheng Y, Walz T. Negative Staining and Image Classification - Powerful Tools in Modern Electron Microscopy. Biol Proced Online. 2004;6:23–34.

892 43. Bush MJ, Bibb MJ, Chandra G, Findlay KC, Buttner MJ. Genes Required for Aerial
893 Growth, Cell Division, and Chromosome Segregation Are Targets of WhiA before
894 Sporulation in *Streptomyces venezuelae*. mBio. 2013 Sep 24;4(5):e00684-13.

895 44. Gallego JJ, Severi E, Chandra G, Palmer T. Identification of novel tail-anchored membrane
896 proteins integrated by the bacterial twin--arginine translocase. Microbiology (Reading).
897 2024 Feb;170(2):001431.

898 45. Zheng SQ, Palovcak E, Armache JP, Verba KA, Cheng Y, Agard DA. MotionCor2:
899 anisotropic correction of beam-induced motion for improved cryo-electron microscopy.
900 Nat Methods. 2017 Apr;14(4):331–2.

901 46. Afanasyev P, Ravelli RBG, Matadeen R, De Carlo S, van Duinen G, Alewijnse B, et al. A
902 posteriori correction of camera characteristics from large image data sets. Sci Rep. 2015
903 Jun 11;5(1):10317.

904 47. P. Afanasyev. CryoEM tools [Internet]. 2023. Available from:
905 https://github.com/afanasyevp/cryoem_tools

906 48. Punjani A, Rubinstein JL, Fleet DJ, Brubaker MA. cryoSPARC: algorithms for rapid
907 unsupervised cryo-EM structure determination. Nat Methods. 2017 Mar 1;14(3):290–6.

908 49. Wagner T, Merino F, Stabrin M, Moriya T, Antoni C, Apelbaum A, et al. SPHIRE-
909 crYOLO is a fast and accurate fully automated particle picker for cryo-EM. Commun Biol.
910 2019 Jun 19;2(1):1–13.

911 50. Scheres SHW. RELION: implementation of a Bayesian approach to cryo-EM structure
912 determination. J Struct Biol. 2012 Dec;180(3):519–30.

913 51. Weiss GL, Medeiros JM, Pilhofer M. In Situ Imaging of Bacterial Secretion Systems by
914 Electron Cryotomography. Methods Mol Biol Clifton NJ. 2017;1615:353–75.

915 52. Mastronarde DN. Automated electron microscope tomography using robust prediction of
916 specimen movements. J Struct Biol. 2005 Oct;152(1):36–51.

917 53. Kremer JR, Mastronarde DN, McIntosh JR. Computer visualization of three-dimensional
918 image data using IMOD. J Struct Biol. 1996 Feb;116(1):71–6.

919 54. Tegunov D, Cramer P. Real-time cryo-electron microscopy data preprocessing with Warp.
920 Nat Methods. 2019 Nov;16(11):1146–52.

921 55. Emsley P, Lohkamp B, Scott WG, Cowtan K. Features and development of Coot. Acta
922 Crystallogr D Biol Crystallogr. 2010 Apr;66(Pt 4):486–501.

923 56. Song Y, DiMaio F, Wang RYR, Kim D, Miles C, Brunette T, et al. High-resolution
924 comparative modeling with RosettaCM. Struct Lond Engl 1993. 2013 Oct 8;21(10):1735–
925 42.

926 57. Adams PD, Afonine PV, Bunkóczi G, Chen VB, Davis IW, Echols N, et al. PHENIX: a
927 comprehensive Python-based system for macromolecular structure solution. Acta
928 Crystallogr D Biol Crystallogr. 2010 Feb;66(Pt 2):213–21.

58. Schindelin J, Arganda-Carreras I, Frise E, Kaynig V, Longair M, Pietzsch T, et al. Fiji - an Open Source platform for biological image analysis. Nat Methods. 2012 Jun 28;9(7):10.1038/nmeth.2019.

59. Ef P, Td G, Cc H, Gs C, Dm G, Ec M, et al. UCSF Chimera - a visualization system for exploratory research and analysis. J Comput Chem. 2004 Oct 2022 May 17];25(13).

60. Goddard TD, Huang CC, Meng EC, Pettersen EF, Couch GS, Morris JH, et al. UCSF ChimeraX: Meeting modern challenges in visualization and analysis. Protein Sci Publ Protein Soc. 2018 Jan;27(1):14–25.

61. Jumper J, Evans R, Pritzel A, Green T, Figurnov M, Ronneberger O, et al. Highly accurate protein structure prediction with AlphaFold. Nature. 2021 Aug;596(7873):583–9.

62. Mirdita M, Schütze K, Moriwaki Y, Heo L, Ovchinnikov S, Steinegger M. ColabFold: making protein folding accessible to all. Nat Methods. 2022 Jun;19(6):679–82.

63. O'Reilly FJ, Graziadei A, Forbrig C, Bremenkamp R, Charles K, Lenz S, et al. Protein complexes in cells by AI-assisted structural proteomics. Mol Syst Biol. 2023 Apr 12;19(4):e11544.

64. Madeira F, Madhusoodanan N, Lee J, Eusebi A, Niewielska A, Tivey ARN, et al. The EMBL-EBI Job Dispatcher sequence analysis tools framework in 2024. Nucleic Acids Res. 2024 Jul 5;52(W1):W521–5.

65. Zhang Y, Wang L, Zhang S, Yang H, Tan H. hmgA, transcriptionally activated by HpdA, influences the biosynthesis of actinorhodin in *Streptomyces coelicolor*. FEMS Microbiol Lett. 2008 Mar;280(2):219–25.